HHS Public Access

Author manuscript

Cancer Discov. Author manuscript; available in PMC 2023 September 01.

Published in final edited form as:

Cancer Discov. 2023 March 01; 13(3): 746–765. doi:10.1158/2159-8290.CD-22-0366.

Mutant NPM1 directly regulates oncogenic transcription in acute myeloid leukemia

Hannah J. Uckelmann[1,#], **Elena L. Haarer**[1], **Reina Takeda**[1], **Eric M. Wong**[1], **Charlie Hatton**[1], **Christian Marinaccio**[1], **Florian Perner**[1], **Masooma Rajput**[1,2], **Noa J. C. Antonissen**[1], **Yanhe Wen**[1], **Lu Yang**[3], **Lorenzo Brunetti**[4,5], **Chun-Wei Chen**[3], **Scott A. Armstrong**[1,#]

[1]Department of Pediatric Oncology, Dana-Farber Cancer Institute, and Division of Hematology/Oncology, Boston Children's Hospital, and Harvard Medical School, Boston, MA, USA

[2]German Cancer Research Center, DKFZ, Heidelberg, Germany

[3]Department of Systems Biology, Beckman Research Institute, City of Hope, Duarte, CA, USA

[4]Department of Medicine and Surgery, University of Perugia, Perugia Italy

[5]Department of Clinical and Molecular Sciences, Marche Polytechnic University, Ancona, Italy

Abstract

The dysregulation of developmental and stem cell associated genes is a common phenomenon during cancer development. Around half of acute myeloid leukemia (AML) patients express high levels of *HOXA* cluster genes and *MEIS1*. Most of these AML cases harbor an NPM1 mutation (NPM1c), which encodes for an oncogene mislocalized from the nucleolus to the cytoplasm. How NPM1c expression in hematopoietic cells leads to its characteristic gene expression pattern remains unclear. Here, we show that NPM1c directly binds to specific chromatin targets, which are co-occupied by the histone methyltransferase KMT2A (MLL1). Targeted degradation of NPM1c leads to a rapid decrease in gene expression and loss of RNA Polymerase II, as well as activating histone modifications at its targets. We demonstrate that NPM1c directly regulates oncogenic gene expression in collaboration with the MLL1 complex and define the mechanism by which MLL1-Menin small molecule inhibitors produce clinical responses in patients with *NPM1*-mutated AML.

INTRODUCTION

The incidence of acute myeloid leukemia (AML) increases with age with cure rates as low as 5 to 10 % in older age groups. Despite the improvements in supportive care and relapse monitoring, many patients still suffer poor outcomes and therapy-related mortality (1). This underscores the need for targeted therapeutic options, which in turn require a deep

Corresponding Authors: Scott A. Armstrong, 450 Brookline Ave, 02215 Boston, Scott_Armstrong@DFCI.Harvard.edu, +1-617-632-3232, **Hannah J. Uckelmann**, 360 Longwood Ave, LC-8201, 02215 Boston, HannahJ_Uckelmann@DFCI.Harvard.edu, +1-617-632-2038.

[#]Co-corresponding Authors.

Author contributions:

S.A.A. and H.J.U. conceived the study and wrote the manuscript with input from all the authors. H.J.U., E.L.H., R.T., E.M.W., M.R., and N.J.C.A. conducted experiments. C.C. and L.Y. generated the CRISPR tiling screening library and analyzed the screen. C.H., Y.W., and C.M. performed bioinformatics analysis for RNAseq, SLAM-seq and ChIPseq experiments. F.P. and L.B. contributed to experimental planning and resources. S.A.A. supervised the study.

mechanistic understanding of the molecular processes that drive leukemogenesis. *NPM1* mutations in AML were first described 16 years ago and represent one of the most frequent genetic abnormalities in these leukemias (2, 3). Mutations in *NPM1* lead to the generation of an additional nuclear export signal (NES) and the loss of the nucleolar localization signal (NoLS) (4). Most functional studies of mutant NPM1 (NPM1c) have focused on identifying interacting proteins that may be evicted from the nucleus to the cytoplasm in tandem with NPM1c. These factors include Arf, CTCF, PU.1, and others (5–7). However, its mechanistic role in leukemia development remains elusive. In particular, there is no insight into whether NPM1c directly drives its very distinct oncogenic gene expression program, which includes *HOXA* and *HOXB* cluster genes, *MEIS1,* and many other self-renewal associated genes. A recent study suggested that NPM1c is recruited to the *HOXA* cluster with the help of nuclear exporter CRM1 (8). However, it remains unclear whether NPM1c is bound to other chromatin sites and more importantly, what the functional consequences of this binding are for gene expression.

Another interesting connection between NPM1c and chromatin is the fact that NPM1c AMLs are highly sensitive to the disruption of the MLL1 histone methyltransferase complex and enzymatic inhibition of the H3K79 methyltransferase DOT1L (9, 10). Small molecule inhibitors that block the interaction between MLL1 and its adaptor protein Menin have been shown to impair binding of MLL1 to a subset of its target genes and to inhibit leukemia cell proliferation and self-renewal (11, 12). Several MLL1-Menin inhibitors are currently in Phase I/II clinical trials and show promising activity in patients with NPM1c AML (9, 13). The effectiveness of these molecules in NPM1c AML prompts the question whether NPM1c and the wildtype MLL complex cooperate directly on chromatin to drive leukemic self-renewal.

Here, we use an endogenously degrader tagged NPM1c leukemia cell line that allows rapid small molecule induced degradation to identify specific global chromatin binding targets of NPM1c and show that it occupies a small number of leukemic self-renewal associated genes (14). We demonstrate that the loss of NPM1c from its targets leads to specific alterations in chromatin, which are accompanied by rapid changes in gene expression and RNA Polymerase II (Pol II) transcriptional activity. We further demonstrate that NPM1c is lost from specific loci after treatment with small molecules that disrupt the MLL1-Menin complex interaction, thus functionally linking targeted epigenetic therapy and NPM1c function. Apart from the presence of the MLL complex, we also show that NPM1c chromatin binding is dependent on multiple factors, including its interaction with CRM1 and the presence of an acidic stretch in its histone binding domain. These findings demonstrate an unexpected direct role for the NPM1c oncoprotein in the control of tumor-promoting transcription.

RESULTS

Genome-wide identification of NPM1c chromatin targets through targeted degradation

To investigate the specificity and functional relevance of NPM1c binding to chromatin, we used a previously developed *NPM1*-mutated leukemia cell line (OCI-AML3-NPM1c-FKBP12) in which only the mutant allele of *NPM1* is modified to produce an endogenously

tagged version of NPM1c fused to the FKBP12 tag (Fig. 1A) (14). This system uses hetero-bifunctional molecules that bind to FKBP12 and recruit the E3 ubiquitin ligase Cereblon (15). The degradation of endogenous NPM1c leads to rapid induction of differentiation and apoptosis within 4 days of treatment with a small molecule degrader (dTAG-13) (Fig. 1B and C, Supplementary Fig. S1A to E). While immunoblotting analysis of nuclear and cytoplasmic fractions of OCI-AML3-NPM1c-FKBP12 cells revealed that the majority of NPM1c protein is localized to the cytoplasm, approximately 10 % of NPM1c resides in the nucleus (Fig. 1D and E). To assess for potential chromatin binding targets of the nuclear fraction of the NPM1c oncoprotein, we took advantage of the endogenous degrader model and performed chromatin immunoprecipitations followed by sequencing (ChIPseq) using a mutant specific NPM1c antibody (NPM1c-Ab) and a total NPM1 antibody (NPM1-Ab), which recognizes both the mutant and the wildtype NPM1 (Fig. 1F). Using two replicates of ChIPseq experiments for each of these different antibodies, we identified a small group of 44 genes that were consistently detected in all four ChIP experiments. To validate that these were indeed specific NPM1c targets, we degraded the endogenous mutant protein for 24 hours of dTAG-13 treatment, where NPM1c was undetectable by immunoblotting (Supplementary Fig. S1F). To make definitive conclusions about the effects of NPM1c on its chromatin binding targets, we decided to use only genes that show a substantial reduction (> 50 %) in signal upon NPM1c degradation. With this, we obtained a total of 33 high confidence NPM1c chromatin target genes which we used to study the effects of NPM1c degradation in detail (Fig. 1G; Supplementary Fig. S2A; Supplementary Table S1 and S2). These genes include many of the characteristically upregulated genes in NPM1c leukemia cells, such as *HOXA* and *HOXB* cluster genes, *MEIS1*, *IRX5, CDK6,* and *CDKN2C* (14, 16). The peaks that were only detected in the total NPM1 samples and not the mutant specific ChIPseq samples are putative NPM1 wildtype targets, which are not lost upon degradation (Supplementary Fig S2B; Supplementary Table S2). We analyzed the peaks detected in our NPM1c-Ab and NPM1-Ab ChIPseq experiments for recurring transcription factor motifs (Supplementary Fig. S3A and B). Our MEME motif analysis revealed a small number of enriched DNA sequences; among these were several homeobox transcription factor motifs and other hematopoietic or developmental factors, such as ZEB1, ETS2, and FLI1. These data confirm that NPM1c is recruited to sites on chromatin that are important for hematopoietic development.

We next wanted to ensure that NPM1c chromatin binding is also found in patient AML samples. We performed ChIPseq experiments using both NPM1c-Ab and total NPM1-Ab in patient derived xenograft (PDX) samples established from two NPM1wt (with *MLL-AF9* or *RUNX1*, *ASXL2*, *TET2,* and *EZH2* mutations) and four NPM1c AML patients (with co-mutations such as *FLT3ITD* and *IDH2*) (Fig. 1H; Supplementary Fig. S4A and B; Supplementary Table S3). Both antibodies identified NPM1c bound to *HOXA/B*, *MEIS1,* and many other targets in NPM1c PDX samples but not *NPM1*-wildtype patient samples (Fig. 1H; Supplementary Fig. S4A and B; Supplementary Table S4). Overall, we found 54 NPM1c targets which were detected in all 4 NPM1c PDX samples and not in the negative controls (Fig. 1H; Supplementary Fig. S4B; Supplementary Table S2 and S4). We compared these PDX specific NPM1c target genes with the ones identified in our OCI-AML3 model and found that half of the OCI-AML3 targets were consistently detected in all 4 PDX

samples, while others were only detected in a subgroup of PDX samples (Supplementary Fig. S4C). Using the publicly available gene expression data from the BEAT AML, Tumor Cancer Genome Atlas (TCGA), and Wouters *et al.* 2009 cohorts, we found that the NPM1c target genes we identified in our PDX samples were also highly expressed in NPM1c versus NPM1-wildtype AML patient samples, demonstrating a strong correlation between NPM1c binding and increased expression of its chromatin target genes in leukemia patients (Fig. 1I and J; Supplementary Fig. S4D to G) (17–19). Therefore, NPM1c binds to chromatin at loci that are highly expressed in human AML samples taken from patients with NPM1 mutant AML.

NPM1c regulates transcription of its chromatin targets

Since we saw a correlation between NPM1c chromatin binding and gene expression in primary patient samples, we wanted to assess the impact of NPM1c binding on the transcriptional activity of its target genes using the NPM1c degradation model. Global gene expression analysis revealed that the majority of NPM1c targets were transcriptionally downregulated after 24 hours of dTAG-13 treatment (Fig. 2A; Supplementary Table S5). Next, we took advantage of the rapid kinetics of the dTAG degradation system and determined the earliest time points at which NPM1c is lost from chromatin. A significant global decrease of NPM1c protein was evident after just 15 minutes of dTAG-13 treatment (Fig. 2B). We confirmed the loss of NPM1c from chromatin by ChIP qPCR and similarly observed an instant decrease of target occupancy of NPM1c within 15 minutes of degradation (Supplementary Fig. S5A). To interrogate the immediate effects of NPM1c loss on transcription, we performed qPCR for *MEIS1* and *HOXA9* using primers that assess processed mRNA levels and observed the first gene expression changes at 1–2 hours post dTAG-13 treatment (Supplementary Fig. S5B). Next, we performed qPCR with primers that detect pre-spliced, newly synthesized RNA. This demonstrated more rapid changes in *HOXA9* and *MEIS1* expression starting at 15 to 30 minutes (Supplementary Fig. S5C). For a global assessment of nascent transcription, we performed SLAM sequencing (SLAM-seq) after 15, 30, 60, 120, and 180 minutes of degradation (Fig. 2C and D; Supplementary Fig. S5D to F; Supplementary Table S6) and observed gene expression changes just 15 minutes after treatment (20). Strikingly, the majority of genes that were more than fifty percent downregulated in the first 15 to 180 minutes after degradation were NPM1c chromatin targets. There were no upregulated genes in the first two hours post degradation in our SLAM-seq analysis. These findings suggest that NPM1c has a direct and rapid effect on gene expression. To further study the effects of NPM1c chromatin binding on transcription, we performed precision run-on sequencing (PRO-seq), which maps the location of active RNA polymerases genome-wide and can be used to map acute changes in Pol II dynamics upon perturbations of transcription (21–23). We found a loss of Pol II activity at NPM1c target genes as quickly as 30 and 60 minutes after degradation (Fig. 2E and F; Supplementary Table S7). Pol II activity was decreased at the TSS as well as the gene body, suggesting that the immediate transcriptional changes in response to NPM1c degradation are caused by an overall loss of Pol II activity, rather than effects on transcriptional pausing or elongation (Fig. 2G and H). Overall, the rapid kinetics of the dTAG system revealed that the binding of NPM1c to chromatin is essential for maintaining

high levels of transcription at its targets, thus establishing a direct role for NPM1c in transcriptional regulation on chromatin.

NPM1c chromatin binding promotes a transcriptionally active chromatin state at its target sites

We next assessed NPM1c's role in maintaining the integrity of chromatin and transcriptional complexes. Analysis of the NPM1c bound regions in OCI-AML3 cells revealed that NPM1c peaks are located mainly at the gene body, as well as the TSS regions rather than on intergenic regions (Supplementary Fig. S6A). In addition, NPM1c peaks largely overlapped with the active histone mark H3K27ac while they rarely have H3K27me3 repressive marks present (Supplementary Fig. S6A). This indicates that NPM1c is bound to actively transcribed genes. Given the drastic changes in transcriptional output upon loss of NPM1c, we next wanted to assess complexes that control transcription and the chromatin state. To determine whether NPM1c degradation affects the transcriptional machinery itself, we performed ChIPseq for RNA Pol II (Pol II) and CDK9, the catalytic subunit of P-TEFb, which phosphorylates Pol II to initiate its release into the elongation phase of transcription (24). Both Pol II and CDK9 binding were significantly reduced at the majority of NPM1c target genes 24 hours post degradation (Fig. 3A to C; Supplementary Table S1). Histone modifications associated with active transcription, such as H3K27ac and H3K9ac, were also strongly reduced at NPM1c target genes after 24 hours of dTAG-13 exposure (Fig. 3A, D, and E). Interestingly, DOT1L, an H3K79 methyltransferase that plays a role in maintenance of gene expression and is important for NPM1c AML proliferation (10), was lost at the majority of NPM1c target sites upon degradation as well (Fig. 3A and F). Global levels of Pol II, CDK9, DOT1L and H3K27 acetylation were only mildly affected by NPM1c degradation (Supplementary Fig. S6B). The decreased occupancy of the transcriptional machinery (CDK9, Pol II), loss of transcription-associated histone acetylation (H3K27ac, H3K9ac), and DOT1L loss are most striking at NPM1c target genes and correlate with their loss in gene expression (Fig. 2A; Fig. 3B to F). The repressive histone modification H3K27me3 remained unchanged at 24 hours by ChIP qPCR (Fig. 3G).

To determine which of these chromatin changes happen most quickly and therefore could be responsible for the rapid gene expression changes, we performed ChIPseq and ChIP qPCR for these different factors after just 1 hour of NPM1c degradation (Supplementary Fig. S6C to F; Supplementary Table S1). At this early time point, we observed that Pol II and CDK9, as well as H3K27ac and H3K9ac, were already significantly reduced. On the contrary, DOT1L and H3K79me2 remained unchanged at this early time point, suggesting that loss of DOT1L occupancy is secondary to loss of transcriptional activity at these loci. In sum, our data suggest that the rapid transcriptional changes induced by NPM1c degradation are primarily caused by a loss of the transcriptional machinery and simultaneous loss of histone acetylation rather than repression of target loci.

The NPM1c acidic stretch is important for NPM1c chromatin recruitment

In order to identify potential domains of NPM1c that are important for its leukemogenic function, we performed a CRISPR-Cas9 based tiling knock-out screen based on the concept that sgRNAs targeting essential domains drop out at higher efficiency than those targeting

non-essential domains (25). We first performed a small pilot screen with 20 sgRNAs across different exons of NPM1 and observed a higher sensitivity to sgRNAs targeting exons 1, 4, 5, and 11 in the mutant NPM1 versus wildtype cells (Supplementary Fig. S7A to D). To achieve better resolution of the essential domains, we performed a pooled library screen containing 156 sgRNAs covering NPM1c, including three NPM1c mutant specific, 40 negative control, and 24 killing control sgRNAs (Fig. 4A; Supplementary Table S8). The screen was performed in single cell clones of NPM1c OCI-AML3 cells, as well as MLL-rearranged MOLM13 cells that express wildtype NPM1, both of which stably express Cas9. Of interest, sgRNAs that target the mutant specific COOH-terminal tail of the protein and the region between amino acids 120 and 150 dropped out most strongly and specifically in OCI-AML3 NPM1c AML cells in two different single cell clones (Fig. 4A; Supplementary Fig. S7E and F). This highly sensitive region contains an acidic stretch (AS2), which has been reported to be important for the histone binding and chaperoning activity of wildtype NPM1 (26, 27). We next tested whether AS2 is required for the binding of NPM1c to chromatin by overexpression in 293T cells of either HA-tagged NPM1c, NPM1wt, or NPM1c where AS2 was deleted (NPM1c-ΔAS2) (Fig. 4B; Supplementary Fig. S8A). Both NPM1c and NPM1c-ΔAS2 show a prominent cytoplasmic localization by fluorescence microscopy and small percentage of overexpressed NPM1c-ΔAS2 is present in the nucleus (Fig. 4C; Supplementary Fig. S8B). ChIPseq analysis revealed that NPM1c-HA is recruited to the *HOXA* Cluster and other sites such as *CDKN1B*, *FOXC1,* and *SP9* in 293T cells (Fig 4D; Supplementary Table S9). Neither NPM1wt-HA nor NPM1c-ΔAS2-HA were detectable on chromatin (Fig. 4D). Gene expression analysis of NPM1c compared to empty control, NPM1wt, and NPM1c-ΔAS2 overexpressing 293T cells showed only very mild upregulation of NPM1c bound genes *HOXA10*, *HOXA13,* and *FOXG1* (Supplementary Fig. S8C and D; Supplementary Table S10). Most other NPM1c bound genes were not transcriptionally upregulated. Therefore, the acidic stretch is essential for chromatin recruitment of mutant NPM1, however, there are additional factors required for NPM1c to activate transcription in 293T cells. Since 293T cells did not recapitulate the same transcriptional response as leukemia cells, we wanted to ensure that the AS2 domain is similarly essential in a more relevant cell type. For this, we stably overexpressed either NPM1c or NPM1c-ΔAS2 in OCI-AML3-NPM1c-FKBP cells and confirmed that NPM1c-ΔAS2 was present in the nucleus (Supplementary Fig. S8E). We then degraded the endogenous NPM1c by 24 hours of dTAG-13 treatment and performed ChIP experiments using NPM1c-Ab to confirm that the AS2 deletion leads to a decrease in binding capacity of NPM1c by ChIP qPCR (Fig. 4E; Supplementary Fig. S8F). The decrease in chromatin occupancy of NPM1c-ΔAS2 was accompanied by a significant reduction in *HOXA1*0 and *MEIS1* expression in NPM1c-ΔAS2 compared to the full-length NPM1c expressing cells (Supplementary Fig. S8G). To test whether AS2 deletion has similar effects on wildtype NPM1, we isolated chromatin fractions from OCI-AML3 cells overexpressing wildtype or mutant NPM1 lacking the AS2 domain (Supplementary Fig. S8H). While removing AS2 led to reduced levels of NPM1c in the chromatin fraction compared to full length NPM1c, wildtype NPM1 lacking AS2 was still present in the chromatin fraction at similar levels as full-length wildtype NPM1. This suggests that NPM1c is more reliant on this particular acidic domain than wildtype NPM1, which seems to require deletion of both AS2 and AS3 to disrupt its binding as shown in previous studies (28–30). These findings demonstrate that mutant and wildtype NPM1 may

engage chromatin via slightly different mechanisms that could potentially be exploited to specifically target the oncogenic form of NPM1.

Nuclear export factor CRM1 is essential for the genome-wide target recruitment of NPM1c

NPM1c is transported from the nucleus to the cytoplasm by nuclear export factor CRM1 (also known as XPO1) (31). A recent study also suggests that CRM1 is involved in the recruitment of NPM1c to *HOXA* and *B* cluster genes (32). Our CRM1 ChIPseq experiments confirm that NPM1c-HA binds to regions with high levels of chromatin-bound CRM1 in 293T cells (Fig. 5A). Similarly, we found high CRM1 loading at NPM1c target genes in leukemia cells (Fig. 5B). Interestingly, the degradation of NPM1c led to a loss of CRM1 chromatin binding at NPM1c target sites and a global reduction of CRM1 protein levels by approximately 50 %, suggesting that the interaction with NPM1c is crucial for the stability of CRM1 (Fig. 5C and D). To determine whether the CRM1-NPM1c interaction is a general requirement for NPM1c chromatin engagement, we tested whether inhibition of the interaction of CRM1 with the NES of NPM1c would disrupt NPM1c binding to all or just a subset of its targets. For this, we treated OCI-AML3 cells with the selective CRM1 inhibitor Selinexor, which blocks the interaction of CRM1 with NES. After only 6 hours of Selinexor treatment, the expression of *MEIS1* and *HOXA9* was significantly reduced (Fig. 5E). Globally, we observed similar gene expression analysis after 6 hours of Selinexor compared to 3 hours of dTag-13 treatment, indicating that the short-term disruption of the CRM1-NES interaction has similar effects as degrading the NPM1c oncogene itself (Supplementary Fig. S9A). Next, we performed ChIPseq analysis to determine if changes in NPM1c chromatin occupancy at NPM1c target genes following Selinexor treatment paralleled the changes observed after NPM1c degradation. Indeed, we observed that the CRM1-NES interaction is generally essential for NPM1c chromatin binding (Fig. 5F and G). Furthermore, CRM1 remained bound to chromatin after Selinexor treatment, confirming that CRM1 by itself is found on chromatin while NPM1c is recruited via the interaction between CRM1 and the NES of NPM1c (Fig. 5F; Supplementary Fig. S9B). To confirm the interaction of NPM1c with CRM1 on chromatin using an alternative approach, we performed immunoprecipitation experiments of endogenous NPM1c from the chromatin fraction of OCI-AML3 cells followed by immunoblot analysis (Fig. 5H). This interaction of CRM1 and NPM1c on chromatin can be disrupted by Selinexor treatment, as shown by our ChIPseq experiment, and confirmed by co-immunoprecipitation experiments from chromatin fractions followed by immunoblotting (Fig. 5F and Supplementary Fig S9C). To gain more insight into the mechanism of interaction between NPM1c and CRM1, we performed co-immunoprecipitation experiments in 293T cells. First, we overexpressed HA tagged NPM1c and NPM1c-ΔAS2 and found that albeit lower expression levels in the input, the ΔAS2 mutant was still pulled down with Flag-tagged CRM1 (Supplementary Fig. S9D). Since we observed a rapid loss of NPM1c chromatin binding after blocking the CRM1-NES interaction using Selinexor, we hypothesized that the presence of the NES in NPM1c itself is important for the CRM1-NPM1c interaction. To test this, we deleted the mutant specific NES in NPM1c and overexpressed full length (NPM1c-HA) or NES deleted NPM1c (NPM1c-ΔNES-HA) in combination with Flag-tagged CRM1 (Supplementary Fig. S9D). NPM1c-ΔNES-HA was pulled down at lower levels than full-length NPM1c and at levels comparable to HA-tagged wildtype NPM1. This suggests that the mutant NES is

important for enhancing the affinity of NPM1c to CRM1. These data in combination with our Selinexor ChIPseq data confirm that the NES of NPM1c mediates the recruitment to CRM1 on chromatin. Overall, we demonstrate that NPM1c chromatin binding and transcriptional activation at NPM1c target sites is dependent on its AS2 domain, as well as its interaction with CRM1 through its NES. Therefore, multiple features of NPM1c are required for its chromatin engagement.

NPM1c is evicted from chromatin at select loci upon Menin-MLL inhibition

We have previously shown that NPM1c leukemias are highly sensitive to the inhibition of the interaction between the lysine 4 histone methyltransferase MLL1 and its adaptor protein Menin, which is essential for MLL1 binding to certain loci, such as *MEIS1* and *IGF2BP2* (9). While Menin-MLL inhibitors are currently in clinical trials for NPM1c patients, we still know very little about the mechanism of action of this potent targeted therapy in NPM1 mutant patients. Interestingly, our newly identified NPM1c target genes include many known MLL-AF9 oncofusion target genes (Supplementary Fig. S10A) (33). Therefore, we wanted to assess whether wildtype MLL1 and mutant NPM1 directly cooperate on chromatin. MLL1 ChIPseq analysis revealed that indeed all NPM1c target genes were co-occupied by high levels of MLL1 (Fig. 6A). Interestingly, when we degrade NPM1c, MLL1 and its complex members Menin and LEDGF are still present on chromatin after 24 hours of dTAG-13 treatment (Supplementary Fig. S10B; Supplementary Table S1). This suggests that NPM1c is recruited to loci where MLL1 is already present. While the MLL1 complex remains in place after NPM1c degradation, many of its common target genes show decreased expression, indicating that NPM1c is needed for maintaining high transcriptional activity of its oncogenic target gene program in leukemia cells (Supplementary Fig. S10C). However, in contrast to CRM1, we were unable to co-precipitate MLL1 from chromatin fractions by NPM1c-IP, which may suggest a more transient or indirect interaction between these two factors on chromatin (Fig. 5H).

Since MLL1 chromatin occupancy does not depend on NPM1c, we hypothesized that NPM1c is dependent on the presence of MLL1 for its binding. To test this, we used the Menin-MLL inhibitor VTP-50469, which selectively disrupts the interaction between Menin and MLL1 and leads to a loss of MLL1 binding from a subset of its targets, which in turn also show decreased gene expression (9, 11). Indeed, we saw a specific loss of NPM1c at loci that showed loss of MLL1 binding, such as *MEIS1*, *IGF2BP2*, *RUNX2, MKX, PHF10, SATB1,* and others (Fig. 6B and C; Supplementary Table S11). These loci also show decreased gene expression in response to VTP-50469 treatment (Fig. 6D). Similar to the NPM1c degradation setting, Pol II, CRM1, and DOT1L are also lost from transcriptionally suppressed loci that lose NPM1c (Fig. 6B; Supplementary Fig. S10D to F; Supplementary Table S11). NPM1c and MLL1 remain bound at the *HOXA* and *HOXB* clusters, which are not transcriptionally suppressed by VTP-50469 treatment (Fig. 6B and C; Supplementary Table S11). Due to the selective mode of action of Menin-MLL inhibition, we did not observe significant global changes in chromatin binding of the chromatin factors assessed with the exception of Menin, which we reported in previous studies (Supplementary Fig. S10G) (9, 11). We validated the selective loss of NPM1c in an *NPM1* mutant PDX model treated *in vivo* with VTP-50496 for 3 or 6 days, confirming that the disruption

of NPM1c chromatin interaction is a relevant phenomenon in AML patient samples as well (Supplementary Fig. S11A; Supplementary Table S4). Total NPM1c protein levels were not affected at these time points (Supplementary Fig. S11B). Finally, we wanted to investigate whether the loss of NPM1c upon Menin-MLL inhibition is also linked to a loss of transcriptional activity. We used Exon-Intron spanning primers for *MEIS1* to determine the earliest transcriptional changes, which occurred 48 hours after VTP-50469 treatment (Supplementary Fig. S11C). We confirmed NPM1c and MLL1 already showed reduced chromatin occupancy at this time point (Supplementary Fig. S11D and E). We then performed PRO-seq at 48 hours of VTP-50469 treatment and observed reduced RNA Pol II transcriptional activity at the TSS and gene bodies of those genes that lost NPM1c, while the ones where it remained bound showed no change in transcriptional activity (Fig. 6E to G; Supplementary Fig. S12A; Supplementary Table S7). In summary, these data show that mutant NPM1c is targeted to loci where the MLL1 complex is bound and depends on the Menin-MLL interaction for binding to a subset of these loci. Since NPM1c degradation does not lead to depletion of MLL1 from its targets but rather a reduction in transcriptional activity, these data also suggest that NPM1c cooperates with MLL1 at their common target sites to enhance transcription.

Menin-MLL and CRM1 inhibitors are both potent agents that are currently in clinical trials for treatment of NPM1c mutant AML (3, 34). We demonstrate here that both are able to disrupt NPM1c chromatin occupancy through distinct mechanisms. We therefore wanted to test whether there is potential for synergy between these two treatment options. In vitro combination treatment experiments showed not only a more rapid induction of myeloid differentiation marker CD11b but also a more complete downregulation of MEIS1, but not HOXA10 expression when both drugs were combined (Fig. 6H and I; Supplementary Fig. S12B to D). These data indicate that interfering with NPM1c chromatin binding through multiple avenues may result in improved therapeutic responses.

DISCUSSION

NPM1 has been implicated in tumorigenesis by overexpression, deletion, mutation, and translocation (35). Cytoplasmic NPM1 mutations are among the most common aberrancies in leukemia. The study of the mechanism of action of NPM1c has been primarily focused on factors that are evicted from the nucleus to the cytoplasm in tandem with the oncogene resulting in a loss-of-function model (7, 36, 37). However, both wildtype and mutant NPM1 have been shown to interact with chromatin (30, 32, 38). The wildtype NPM1 protein has also been shown to relocalize to the nucleoplasm under certain stress conditions, be recruited to sites of DNA damage, and play a role in DNA repair (39, 40). A recent study further suggests that wildtype NPM1 interacts with chromatin in late S-phase of the cell through interaction with chromatin binding factors PRC2 and MCM2 (30). These examples of transient recruitment to chromatin may explain why wildtype NPM1 chromatin binding has not been well characterized concerning its target specificity except for its potential role in regulating ribosomal DNA repeat binding transcription in the nucleolus (28). In contrast, mutant NPM1 has recently been suggested to be bound to HOXA and B cluster genes (32). However, the genome-wide target specificity of mutant NPM1 chromatin binding and its functional consequences in normal and malignant cell types remain poorly understood. In

this study, we uncover a previously unappreciated role for mutant NPM1 in transcriptional activation of a network of leukemia self-renewal associated genes through direct chromatin interaction. Our studies reveal that NPM1c mediates an active chromatin state, binding of Pol II, and the transcriptional activity of specific target genes. We also show that NPM1c acts in concert with the histone methyltransferase MLL1 to enhance MLL target gene transcription in leukemic cells. NPM1c shares many overlapping target genes with MLL-fusion genes and both oncogenes have similar dependencies on epigenetic modifiers such as DOT1L, HBO1, and MOZ (10, 41–43). We recently used targeted degradation to show that the MLL-AF9 oncogene can directly regulate transcription and induce rapid chromatin changes, similar to what we observed in the case of NPM1c (33). Since we see a similar locus specific disruption of the transcriptional machinery and chromatin landscape, these oncoproteins may influence a more general oncogenic mechanism that drives aberrant transcription. However, NPM1c chromatin recruitment by itself does not seem sufficient to drive gene expression since chromatin binding in 293T cells only has subtle effects on transcriptional output. This suggests that NPM1c acts in concert with other factors on chromatin, such as MLL1, to enhance existing transcriptional activity and take on a similar role as MLL-fusion partners.

The specificity of chromatin binding of epigenetic readers, writers, and erasers depends on a combination of DNA, histone, and protein-protein interactions, which allows for the specificity to certain loci that can be modulated in different cellular contexts. While we detected some transcription factor binding motifs in NPM1c bound regions, our data overall suggest that the chromatin recruitment is not solely based on DNA sequence. There is a core group of NPM1c target genes which we detected in OCI-AML3 cells and all four NPM1c AML patient derived samples we tested, however, there are also NPM1c targets that occur only in a subset of these samples. This suggests that NPM1c binding is regulated by a combination of different factors, which can modulate its binding pattern. Our data reveal that to bind chromatin, NPM1c requires the interaction with CRM1 and the presence of its acidic region AS2, which has been shown to be important for the histone binding of NPM1. While the NPM1c-ΔAS2 deletion mutant was still able to interact with CRM1, it showed a substantial loss of chromatin binding capacity in 293T and OCI-AML3 cells. In addition, our data strongly suggest that the presence of histone methyltransferase MLL1 is a prerequisite for NPM1c chromatin recruitment in leukemia cells. Since we were not able to show a direct interaction between MLL and NPM1c, this interaction seems to be either weak or indirect, such as through chromatin modifications or interactions with MLL complex components and associated epigenetic complexes.

While Menin-MLL inhibition has been shown to be a powerful tool in the treatment of NPM1c AML, the mechanism of action of this drug in these MLL wildtype leukemias was previously unclear. Our studies show that NPM1c enhances the transcriptional output at MLL target sites and that the disruption of the Menin-MLL interaction leads to a loss of NPM1c from chromatin, demonstrating that this inhibitor has a direct effect on the oncogene’s function. We hypothesize that NPM1c is recruited to chromatin targets where MLL1 is already loaded when it is first expressed in a healthy hematopoietic stem or progenitor cell and enhances transcription at its target genes. In the context of healthy hematopoiesis, many NPM1c target genes are expressed in the stem cell compartment and

are downregulated during differentiation. Increased expression of these target genes, such as *HOXA/B* cluster genes and *MEIS1,* in inappropriate cell types has previously been shown to corrupt normal hematopoietic development and cause leukemia (44, 45). Our data indicate that NPM1c drives leukemogenesis by maintenance of enhanced transcriptional output at specific developmental loci, leading to an aberrantly high expression of oncogenic stem cell programs in hematopoietic progenitor cells, thereby blocking their differentiation. Our data further suggest that disrupting NPM1c binding at essential target genes, such as *MEIS1,* through Menin-MLL inhibition leads to decreased expression, reduces leukemic self-renewal capacity, and in turn allows cells to undergo differentiation (9).

The fact that NPM1c is recruited to a specific subset of genes and enhances their transcription may explain the characteristic gene expression pattern observed in NPM1c mutant patients. We show that the presence of NPM1c is important for the activity of the transcriptional machinery and the maintenance of active chromatin marks at its target loci. However, previous studies have also shown that NPM1c is involved in mislocalizing nuclear and chromatin bound factors to the cytoplasm, leading to a loss of function of these factors (3). For example, NPM1c was suggested to disrupt differentiation pathways by exporting transcription factor PU.1 and to interfere with chromatin looping at the HOXA cluster through CTCF mislocalization (5, 7). We therefore believe that a combination of aberrant nuclear export and direct effects of NPM1c on its chromatin targets are likely to be involved in the process of malignant transformation of hematopoietic cells.

In summary, our data show that the prominent stem-cell like gene expression pattern observed in NPM1c AML is in large part a direct consequence of the binding of NPM1c to chromatin. These findings improve our understanding of current targeted therapy options for NPM1c AML and shift our focus of the study of this oncogene from the cytoplasm to the nucleus. Understanding the important role of NPM1c on chromatin and its interplay with other epigenetic complexes will allow for the more targeted development of small molecules that target chromatin and transcriptional complexes as potential therapeutic approaches in this and other cancers.

METHODS:

Data reporting.

No statistical methods were used to predetermine sample size. The experiments were not randomized and the investigators were not blinded to allocation during experiments.

Animals studies.

All animal experiments were performed with the approval of Dana-Farber Cancer Institute's Institutional Animal Care and Use Committee (IACUC). For PDX studies, immunodeficient (NOG - EF NOG-sp/sp;ko/ko) mice (Taconic) were used as recipient mice. Samples for patient derived xenotransplantation were obtained from PRoXe (www.proxe.org) depository(46). $1–10\times10^5$ cells were transplanted into unconditioned immunodeficient NOG mice (Taconic). The percentage of human CD45+ cells in peripheral blood was analyzed weekly by FACS. When median engraftment reached >50 % of hCD45 cells in peripheral

blood, the mice were randomized into 2 groups and treated with either 0.1 % VTP-50469 120mg/kg spiked-in or control chow for the indicated numbers of days.

Cell culture.

Human cell lines were acquired from American Type Culture Collection (ATCC) or Deutsche Sammlung von Mikroorganismen und Zellkulturen (DSMZ) and were cultured in RPMI (OCI-AML3, MOLM13) or DMEM (293T) supplemented with 10 % FBS and 1xpenicillin/streptomycin (Gibco) at 37°C and 5 % CO_2. Human cell lines OCI-AML3 carrying endogenously tagged NPM1 Type A mutant allele were a generous gift from Margaret A. Goodell. For the degradation of endogenous NPM1c, cells were treated with 500 nM dTAG-13 (a generous gift from Behnam Nabet). OCI-AML3 cells were treated with 330 nM VTP-50469 or 100 nM Selinexor, except for experiments assessing synergy of VTP-50469 and Selinexor. Concentrations for synergy experiments are indicated in the Figure Legends.

Transfection and transduction.

HEK293T cells were transiently transfected with 10 μg of plasmid per 10 cm plate using X-tremeGene transfection reagent (Millipore) and harvested for ChIP and immunoblotting at approximately 28 hours post-transfection or for co-immunoprecipitation studies at approximately 48 hours post-transfection as described below. For NPM1c-ΔAS2 cloning, gblocks encoding human NPM1c or human NPM1c-ΔAS2 and containing EcoRI restriction sites were cloned into the EcoRI-digested pLeGO-iC2-IRES-mCherry vector (Addgene, 27345). For virus production, HEK293T cells were co-transfected with 10 μg of lentiviral expression vector, 8 μg of packaging vector (psPAX2), and 2 μg of envelope vector (pMD2.G) per 10 cm plate using X-tremeGene transfection reagent (Millipore). Viral supernatant was filtered through 0.45 μm 48 hours post-transfection. For transduction, 300,000 OCI-AML3-NPM1c-FKBP cells were spin infected with 3 ml of unconcentrated viral supernatant with 1 μg/ml polybrene (Millipore) for 2 hours at 2500 rpm at 37°C. Transduction efficiency, or % PE-positive cells, was measured approximately 72 hours post-transduction and prior to harvesting by FACS. For ChIP, RT-qPCR, and immunoblotting experiments using pLeGO-iC2-NPM1c-IRES-mCherry and pLeGO-iC2-NPM1c-ΔAS2-IRES-mCherry transduced OCI-AML3-NPM1c-FKBP cells, cells were treated with 500 nM dTAG-13 for 24 hours prior to harvesting to degrade endogenous NPM1c.

CRISPR tiling screen.

Cas9 expressing OCI-AML3 or MOLM13 cells were infected with the CRISPR library at 15–20 % RFP transduction efficiency and selected by puromycin (1 μg/ml; Gibco). The selected cells were then subcultured every four days for a total of 14 days. Genomic DNA from each screen culture was collected at the start (day 0) and end (day 14) timepoints. The integrated sgRNA in each sample was PCR-amplified (NEBNext Ultra II Q5; NEB) using primers DCF01 5′-CTTGTGGAAAGGACGAAACACCG-3′ and DCR03 5′-CCTAGGAA-CAGCGGTTTAAAAAAGC-3′ for high-throughput sequencing (NextSeq550, Illumina). To quantify sgRNA reads, 20-nucleotide sequences that matched the sgRNA backbone structure (5′ prime CACCG and 3′ prime GTTT) were extracted and mapped to the library sgRNA

sequences using Bowtie2. The frequency for individual sgRNAs was calculated as the read counts of each sgRNA divided by the total read counts matched to the library. The CRISPR tiling score was defined as a log10-fold change in the frequency of individual sgRNAs between the start (day 0) and end (day 14) of the screened samples and normalized by the median score of the negative control sgRNA (defined as 0.00; sgRNA targeting non-essential sequences) and the median score of the killing control sgRNA (defined as −1.00) within the screen data. The CRISPR tiling score was further interpolated by Gaussian kernel smoothing in R. For the single sgRNA pilot screen, cells were transduced at 20–70% RFP and monitored every 3 days for % RFP by FACS.

Differentiation and apoptosis assays.

For differentiation studies, cells were stained with APC-conjugated CD11b (BioLegend) and DAPI. For apoptosis studies, cells were harvested following dTAG-13 treatment and stained with PE- or APC-conjugated Annexin V according to the manufacturer's instructions (eBioscience). Cells were counter-stained with Propidium Iodide. Samples were then analyzed using an LSR Fortessa flow cytometer (BD Biosciences). Data were analyzed with FlowJo software (Tree Star).

Immunoblotting.

Human cells were washed twice in cold PBS and lysed in 1X Cell Lysis Buffer (CST) supplemented with 1X protease inhibitor cocktail. The samples were mixed with 1X LDS Sample Buffer (Invitrogen) and denatured for 10 min at 95°C. Bone marrow cells harvested from PDX samples were washed twice in cold PBS, lysed directly in 1X Laemmli Sample Buffer (BioRad), and denatured for 10 min at 95°C. Samples were loaded onto 4–12 % Bis-Tris gels (Thermo Fisher) with a protein ladder (BioRad). Proteins were separated by electrophoresis for 2 hours and then transferred onto nitrocellulose membranes using the iBlot 2 dry transfer system (Thermo Fisher). The membranes were blocked in 5 % dry milk in TBS-T for 1 hour and incubated overnight at 4°C with anti-HA (CST), anti-FLAG (CST), anti-NPM1c (Thermo Fisher), anti-Total NPM1 (Thermo Fisher), anti-Total Histone 3 (Abcam), anti-GAPDH (CST), and anti-Vinculin (CST). The next day membranes were washed in TBS-T and treated with IRDye-680/800- (LI-COR) or horseradish peroxidase-conjugated (CST) secondary antibodies for 1 hour. Infrared and chemiluminescent bands were visualized using a LI-COR Odyssey CLx Imaging System or a BioRad ChemiDoc Imaging System, respectively. Band intensities were measured using LI-COR Image Studio software and densitometries of proteins-of-interest were normalized to Vinculin or GAPDH loading controls.

Cellular fractionation.

Approximately 5 million OCI-AML3-NPM1c-FKBP cells were harvested, washed once in PBS, and centrifuged at 300 g for 5 min. The resulting pellet was lysed with 100 µl of ice-cold cytosolic lysis buffer (50 mM HEPES pH 7.5, 140 mM NaCl, 1 mM EDTA pH 8.0, 10 % glycerol, 0.5 % NP-40, 0.25 % Triton-X-100, and 1 mM DTT supplemented with 1X protease inhibitor cocktail). The lysate was centrifuged at 1,100 g for 2 min at 4°C, and the resulting supernatant was transferred to a separate tube as the cytosolic fraction. The remaining pellet was washed two more times with cytosolic lysis buffer and

re-centrifuged. The resulting pellet was lysed with 100 µl of ice-cold nuclear lysis buffer (500 mM Tris-HCl pH 7.5 and 500 mM NaCl supplemented with 1X protease inhibitor cocktail and 3 µl of Micrococcal Nuclease (300 units, Thermo Fisher)). The nuclear lysate was then vortexed for 15 sec, incubated on ice for 30 min, incubated at room temperature for 15 min, and vortexed for 15 sec. The nuclear cytosolic lysates were then centrifuged at 20,000 g for 10 min at 4°C. The resulting supernatants were transferred to separate tubes and protein concentrations of the soluble cytosolic and nuclear fractions were measured via BCA assay (Thermo Fisher). The total number of µg contained in each fraction was found by multiplying the volume lysed in by the concentration of each fraction as determined by the BCA assay. 40 µg of each fraction were loaded per lane for immunoblotting analysis. Band intensities of NPM1c, Total NPM1, Vinculin, and Histone 3 protein were measured and divided by 40 µg to determine the band intensity per 1 µg. The band intensity per 1 µg value was then multiplied by the total number of µg per fraction to extrapolate the total band intensity of each protein-of-interest in each fraction. To determine the proportion of each protein-of-interest in the cytosolic vs. nuclear fraction, the total band intensity of each protein-of-interest in the cytosolic fraction or nuclear fraction, respectively, was divided by the sum of the total band intensity of each protein-of-interest in the cytosolic and nuclear fraction.

Co-Immunoprecipitation studies.

For 293T co-IPs, one confluent 10 cm plate was harvested per co-IP, washed once in PBS, and lysed in 250 ul of 20 mM Tris-HCl (pH 7.5), 150 mM NaCl, 0.5% NP-40, 0.5% Triton-X-100, and 2 mM EDTA supplemented with 1x protease inhibitor cocktail. For OCI-AML3 co-IPs, 30 million cells were harvested as previously described (47). Anti-FLAG (Sigma) and anti-NPM1c (Thermo Fisher) were conjugated to protein-G and protein-A magnetic beads (Dynabeads), respectively, on a rotator at 4°C. Antibody-labeled beads were then added to the lysates. Following incubation, beads were placed on a magnet and eluted in 1X Laemmli Sample Buffer (BioRad).

Fluorescence microscopy.

For microscopy analysis of NPM1c-GFP, NPM1wt-GFP, and NPM1c-ΔAS2-GFP, 293T cells were plated and transfected on glass cover slips in a 24-well format with 250 ng of plasmid per well using X-tremeGene transfection reagent (Millipore). Approximately 28 hours post-transfection, cells were washed with PBS and fixed with BD cytofix cytoperm (Thermo Fisher) for 10 min and nuclei were stained with DAPI. Images were acquired on a Ti2 inverted microscope fitted with a CSU-W1 spinning disk confocal head. Z-stacks were collected to cover the whole volume of cells at a spacing of 0.6 µm using a Zyla 4.2 sCMOS camera (Andor), with a 100×/1.45 NA Plan Apochromat oil immersion objective (Nikon). NIS-Elements AR software (Nikon) was used for the acquisition. Maximum intensity projections from all Z-stacks captured are shown in the figures. Image processing was conducted using ImageJ/Fiji software. For microscopy quantifications, cells were scored into cytosolic, nuclear, or both categories based on GFP localization and divided by the total number of cells analyzed to calculate the % of cells with GFP localized to the cytoplasm, nucleus, or both the cytoplasm and nucleus.

RNA isolation and RT-qPCR analysis.

RNA was isolated using the RNeasy Mini Kit (Qiagen) according to manufacturer's instructions and DNase treatment (Qiagen) was performed on the column. RNA was reverse transcribed with the SuperScript™ First-Strand Synthesis System (Invitrogen). For RT-qPCR, the ViiA 7 Real-Time PCR system (Applied Biosystems) was used with 384-well plates. Taqman gene expression assays (Applied Biosystems) were used for real-time quantitative PCR. GAPDH was used as the housekeeping gene for normalization. Relative gene expression was calculated by the comparative ΔΔ cycle threshold method. SYBR green gene expression assays (Applied Biosystems) were used for real-time quantitative PCR where indicated in the Figure Legends. For Intron/Exon RT-qPCRs, cDNA synthesis reactions were set up with and without Reverse Transcriptase to assess contaminating genomic DNA. GAPDH was used as the housekeeping gene for normalization. Relative gene expression was calculated by the comparative ΔΔ cycle threshold method. Oligos used are summarized in Supplementary Table S12. For ChIP-qPCRs, the ViiA 7 Real-Time PCR system (Applied Biosystems) was used with 384-well plates using SYBR green (Applied Biosystems).

RNA sequencing.

For RNA-seq experiments, RNA was isolated as described above. RNA quality for RNA sequencing was checked on the Agilent TapeStation (Agilent) and quantified by Qubit (ThermoFisher). RNA (1 μg) was used to make Illumina compatible libraries by doing Poly-A tail selection and library preparation using the NEBNext UltraTM RNA Library Prep Kit for Illumina (New England Biolabs). Sequencing was done using the Illumina Next Gen Sequencing NextSeq platform (Illumina) with 20–30 million 37 bp, paired-end reads.

SLAM-seq.

SLAM-seq was performed using the Lexogen SLAM-seq Metabolic Labeling kit. OCI-AML3-NPM1c-FKBP12 cells were plated at 5×10^6 cells/mL in 10 % RPMI and were pre-treated either with dTAG-13 (500 nM) or 0.1 % DMSO for 15, 30, 60, 120, or 180 minutes. After pre-treatment, cells were incubated with 4SU (Lexogen) at a final concentration of 100 μM and were incubated with continuous dTAG-13/DMSO treatment for 60 min at 37°C / 5 % CO2. Upon addition of 4SU, cells were kept away from light. Cells were harvested at 300 g for 5 min at 4°C, washed with PBS and the RNA was extracted from the cell pellet using QIAshredders (Qiagen) and RNeasy Plus Mini Kit (Qiagen) according to the manufacturer's protocol. 5 ug of the extracted RNA was Iodoacetamide treated according to the manufacturer's instructions (Lexogen). Libraries were prepared using 500 ng RNA and the QuantSeq 3' mRNA-Seq Library Preparation kit (Lexogen). Sequencing was done using the Illumina Next Gen Sequencing NextSeq platform (Illumina) with 20–30 million 75 bp, single-end reads.

PRO-seq.

15 million cells were harvested and washed once with ice cold PBS in 50 mL conical tubes. Cell pellets were resuspended in 250 μl wash buffer (10 mM Tris-Cl, pH 8.0, 10 mM KCl, 250 mM Sucrose, 5 mM MgCl2, 1 mM EGTA, 10 % (v/v) Glycerol, supplemented freshly

with 0.5 mM DTT, 0.2 μL/mL RNase inhibitor and protease inhibitor) to get single-cell suspensions. 10 mL permeabilization buffer (10 mM Tris-Cl, pH 8.0, 10 mM KCl, 250 mM Sucrose, 5 mM MgCl2, 1 mM EGTA, 0.1 % (v/v), Igepal CA-630, 0.05 % (v/v) Tween-20, 10 % (v/v) Glycerol, supplemented freshly with 0.5mM DTT, 0.2 μL/mL RNase inhibitor and protease inhibitor) were added and samples were incubated on ice for 5 min. Cells were spun down and pellets were washed in 10 ml of wash buffer. Cells were spun again and resuspended in freezing buffer (50 mM Tris-Cl, pH 8.0, 40 % (v/v) glycerol, 5 mM MgCl2, 1.1 mM EDTA, supplemented freshly with 0.5 mM DTT and 1 μL/mL RNase inhibitor). Cells were counted and permeabilization was visualized using trypan blue. 5 million permeabilized cells were snap-frozen in 500 μl freezing buffer in liquid nitrogen and stored at −80°C. All subsequent steps were performed by the Nascent Transcriptomics Core at Harvard Medical School, Boston, MA. Aliquots of frozen (−80°C) permeabilized cells were thawed on ice and pipetted gently to fully resuspend. Aliquots were removed and permeabilized cells were counted using a Luna II, Logos Biosystems instrument. For each sample, 1 million permeabilized cells were used for nuclear run-on, with 50,000 permeabilized *Drosophila* S2 cells added to each sample for normalization. Nuclear run on assays and library preparation were performed essentially as described in Reimer et al.(48) with modifications noted: 2X nuclear run-on buffer consisted of (10 mM Tris (pH 8), 10 mM MgCl2, 1 mM DTT, 300 mM KCl, 20 μM/ea biotin-11-NTPs (Perkin Elmer), 0.8 U/μL SuperaseIN (Thermo), 1 % sarkosyl). Run-on reactions were performed at 37°C. 5’ and 3’ adapters have the same sequences as used in Reimer et al. except that random hexanucleotide unique molecular identifier (UMI) sequences were added to the 3’ end of the 5’ adapter and 5’ end of 3’ adapter respectively. Adenylated 3’ adapter was prepared using the 5’ DNA adenylation kit (NEB) and ligated using T4 RNA ligase 2, truncated KQ (NEB, per manufacturer’s instructions with 15 % PEG-8000 final) and incubated at 16°C overnight. 180 μL of betaine buffer (1.42 g of betaine brought to 10 mL with binding buffer) was mixed with ligations and incubated 5 min at 65°C and 2 min on ice prior to addition of streptavidin beads. After T4 polynucleotide kinase (NEB) treatment, beads were washed once each with high salt, low salt, and blocking oligo wash (0.25X T4 RNA ligase buffer (NEB), 0.3 μM blocking oligo) solutions and resuspended in 5’ adapter mix (10 pmol 5’ adapter, 30 pmol blocking oligo, water). 5’ adapter ligation was per Reimer but with 15 % PEG-8000 final (48). Eluted cDNA was amplified 5-cycles (NEBNext Ultra II Q5 master mix (NEB) with Illumina TruSeq PCR primers RP-1 and RPI-X) following the manufacturer’s suggested cycling protocol for library construction. A portion of preCR was serially diluted for test amplification to determine optimal amplification of final libraries. Pooled libraries were sequenced using the Illumina NextSeq platform.

ChIPseq.

Following the appropriate drug treatment, cells were washed twice in cold PBS. For total NPM1, CRM1, CDK9, and RNA Pol II ChIPs, cells were double crosslinked, first with 2 mM disuccinimidyl glutarate (ThermoFisher) for 30 min at room temperature, then spun down at 600 g for 5 min and subsequently crosslinked in 1 % methanol-free formaldehyde (ThermoFisher) for 8 min at room temperature. All other ChIPs were crosslinked with 1 % methanol-free formaldehyde (ThermoFisher) for 10 min at room temperature. Following crosslinking, cells were quenched using 100 mM Tris pH 8.0 and 250 mM Glycine and

washed twice with room temperature PBS. 20 million cells per mL were then lysed using 50 mM Tris-HCl pH 8.0, 100 mM NaCl, 5 mM EDTA, 1 % SDS and chromatin was collected by centrifugation at 15,000 g for 10 min. Drosophila melanogaster S2 cells were used for spike-in controls. Chromatin from 20 million cells was then resuspended in 1 mL 66 mM Tris-HCl pH 8.0, 100 mM NaCl, 5 mM EDTA, 1.7 % Triton X-100, 0.5 % SDS and sheared using an E100S sonicator (Covaris) to chromatin fragments of 200–400 base-pair DNA size. 5 μL of sonicated chromatin was de-crosslinked with 100 mM NaHCO3, 100 mM NaCl, 1 % SDS in a total volume of 50 μL and was incubated at 65°C for 4–6 hours. Following de-crosslinking, DNA was purified with AMPure XP beads (Beckman Coulter). Input DNA fragments were run on a TapeStation 4200 (Agilent), using D5000 Tape and Reagents (Agilent) to ensure proper shearing, and quantified using Qubit (ThermoFisher). Sheared chromatin from 20 million cells was used in each immunoprecipitation using the following antibodies: anti-NPM1c (Thermo Fisher), NPM1 total (Thermo Fisher), HA (CST), Menin (Bethyl), CDK9 (Santa Cruz), DOT1L (CST), RNA Pol II (CST), LEDGF (Bethyl), CRM1 (CST), and KMT2A/MLL1 (Bethyl) (Supplementary Table S13). Sheared chromatin from 10 million cells was used in each immunoprecipitation using the following antibodies: anti-H3K79me2 (CST), H3K27ac (Abcam), H3K9ac (Abcam), and H3K27me3 (Abcam). Antibodies were conjugated to protein-A or protein-G magnetic beads (Dynabeads) for 2–4 hours on a rotator at 4°C with 0.5 μg/μL BSA (Invitrogen). Subsequently, antibody-labeled beads were added to the sheared chromatin, which was then incubated on a rotator at 4°C overnight. Immunoprecipitated DNA fragments were eluted and de-crosslinked in 100 mM NaHCO3, 100 mM NaCl, 1 % SDS, and incubated at 65°C overnight. Following de-crosslinking, DNA was purified with AMPure XP beads (Beckman Coulter). DNA fragments were quantified by TapeStation 4200 (Agilent) using HSD1000 Tape and Reagent (Agilent) and Qubit (ThermoFisher). 1–10 ng of DNA was used in preparation of Illumina compatible libraries using SMARTer ThruPLEX DNA-Seq Kit (Takara) followed by sequencing using NextSeq550 (Illumina) to obtain 20–30 million 37 bp, paired-end reads.

Gene set enrichment analysis.

Gene set enrichment analysis was performed using GSEA v3.0 software with 1,000 gene set permutations. Gene sets used were NPM1c Target genes listed in Supplementary Table S2. Expression data was used from the following publicly AML expression datasets: Tumor Cancer Genome Atlas (TCGA) and Wouters et al. (GSE14468, 526 AML samples), Beat AML (451 samples)(17–19). Significance cut-offs were assessed on the basis of the GSEA standard recommendations: absolute NES ≥ 1, P ≤ 0.05, Benjamini–Hochberg FDR ≤ 0.25. Heatmaps of NPM1c target gene expression in these three data sets were generated using the GSEA v3.0 software. For gene expression heatmap a Z-score normalization was performed on the normalized RNA-seq read counts across samples for each gene. Z-scores are computed on a gene-by-gene (row-by-row) basis by subtracting the mean and then dividing by the standard deviation.

Bioinformatics analysis.

For ChIP-Seq, raw Illumina sequencer output was converted to FASTQ format using bcl2fastq (v2.20.0.422). A summary of all total and mapped reads of ChIPseq samples

used in this study is shown in Supplementary Table S14. Reads (paired-end 37-mers) were aligned to the human (Gencode GRCh38/hg38) genome using STAR (v2.7.5a; params --alignIntronMax 1 --alignEndsType EndToEnd -- alignMatesGapMax 2000 for ChIPseq analysis), sorted and duplicates marked/removed with picard pipeline tools (v2.9.4). Final "deduped" .BAM files were indexed using SAMtools (v1.95). ChIP-seq data visualizations were produced using IGVtools (TDF signal pileups; v2.3.75) and deeptools (tornado plots; v3.1.3; regions around central points of control sample MACS2 peaks plotted using referencePoint option and k=1). ChIPseq peaks were called using MACS2 with appropriate input samples used as controls. Signal within TSS regions (defined as 1kb upstream from transcription start site to 3kb downstream, using the orientation of the associated gene) and MACS2 peak intervals was determined using the bedtools (v2.28.0) coverage function. Raw read counts were converted to reads per kilobase of interval region (rpk) format; where treated/control sample rpk signal ratios were calculated, treated sample rpk values were first normalized using the ratio of hg38-aligned reads between "deduped" treated and control samples.

For RNAseq, raw Illumina sequencer output was converted to FASTQ format using bcl2fastq (v2.20.0.422). Reads (paired-end 37-mers) were aligned to the human (Gencode GRCh38/hg38) genome using STAR (v2.7.5a), sorted and duplicates marked/removed with picard pipeline tools (v2.9.4). Final "deduped" .BAM files were indexed using SAMtools (v1.95). RNA-seq data visualizations were produced using IGVtools (TDF signal pileups; v2.3.75). Raw per-gene counts were calculated with HTSeq (htseq-count, v0.6.1pl). Differential RNA-seq expression was calculated using the BioConductor DESeq2 package (v1.24,0), using raw unnormalized per-gene counts from deduplicated BAMs.

For SLAMseq, SLAMseq FASTQ files were analyzed using the Slamdunk pipeline(49). Differential SLAMseq expression was calculated using the BioConductor DESeq2 package (v1.24,0), using Slamdunk converted counts.

For PRO-seq data analysis all custom scripts described herein are available on the AdelmanLab Github (https://github.com/AdelmanLab/NIH_scripts). Dual, 6nt Unique Molecular Identifiers (UMIs) were extracted from read pairs using UMI-tools [10.1101/gr.209601.116]. Read pairs were then trimmed using cutadapt 1.14 to remove adapter sequences and low-quality 3' bases (--match-read-wildcards -m 20 -q 10). The paired end reads were then mapped to a combined genome index, including both the spike (dm6) and primary (hg38) genomes, using BWA-MEM (-L 100,5) [arXiv:1303.3997v2]. Inserts shorter than 25nt were removed. The remaining read pairs were then separated based on the genome (i.e. spike vs primary) to which they mapped, and both these spike and primary reads were independently deduplicated, again using UMI-tools. Reads mapping to the hg38 reference genome were separated according to whether they were R1 or R2, sorted via samtools 1.3.1 (-n), and subsequently converted to bedGraph format using a custom script (bowtie2stdBedGraph.pl). We note that this script counts each read once at the exact 3' end of the nascent RNA. Because R1 in PRO-seq reveals the position of the RNA 3' end, the "+" and "−" strands were swapped to generate bedGraphs representing 3' end positions at single nucleotide resolution. Annotated transcription start sites were obtained from human (GRCh38.99) GTFs from Ensembl. After removing transcripts with

{immunoglobulin, Mt_tRNA, Mt_rRNA} biotypes, PRO-seq signal in each sample was calculated in the window from the annotated TSS +/−150 nt, using a custom script, make_heatmap. Given good agreement between replicates and similar return of spike-in reads, bedGraphs were merged within conditions, and depth-normalized, to generate bigWig files binned at 10bp. All windows are relative to the TSS unless otherwise noted. To select gene-level features for differential expression analysis, and for pairing with PRO-seq data, we assigned a single, dominant TSS and transcription end site (TES) to each active gene. This was accomplished using a custom script, get_gene_annotations.sh (available at https://github.com/AdelmanLab/GetGeneAnnotation_GGA), which uses RNA-seq read abundance and PRO-seq R2 reads (RNA 5' ends) to identify dominant TSSs, and RNA-seq profiles to define most commonly used TESs. RNA-seq and PRO-seq data from all conditions were used for this analysis, to comprehensively capture gene activity in these samples. Reads were summed within the +250 to TES window for each active gene using the make_heatmap script (https://github.com/AdelmanLab/NIH_scripts). DEseq2, using the Wald test, was used to determine statistically significant differentially expressed genes [10.1186/s13059-014-0550-8]. Unless otherwise noted, the default size factors determined by DEseq2 were used. For "Non-NPM1c Target genes", genes were first selected based on having abs(log2FC) <= log2(1.3) and padj > 0.1 across all comparisons made in the RNA/SLAM-seq differential expression analyses. Subsequent filtering included retaining only protein-coding or lncRNA genes, only genes at least 1kb in length, and only genes with at least 1 count/kb within +250 to TES for all PRO-seq samples. Average metagene plots of PRO-seq read density from TSS to TES of indicated gene groups were generated using make_heatmap as described above. Each gene was divided from TSS to TES positions into 50 bins of equal length, and read density calculated in each length scaled bin, as reads per kilobase. Read density flanking each gene were also calculated (2kb upstream of TSS and 2kb downstream of TES), in 10 bins of 200 bp each. Average values for each gene group are shown. PRO-seq data visualizations were produced using IGVtools (TDF signal pileups; v2.3.75).

Statistical analysis.

Statistical analyses were performed using GraphPad Prism software as noted in the Figure Legends. P-values for data sets were determined using Mann-Whitney tests unless otherwise noted. P-values <0.05 were considered statistically significant.

Supplementary Material

Refer to Web version on PubMed Central for supplementary material.

Acknowledgements:

We thank all members of the Armstrong lab for invaluable discussions and Jennifer Perry for her valuable feedback on this manuscript. We would like to thank Stamatis Papathanasiou for his help with fluorescence microscopy and image processing. We thank Margaret Goodell for generously sharing her OCI-AML3-NPM1c-FKBP12 cells line with us and Nathanael Gray for graciously supplying the dTAG-13 compound for these studies. The authors would like to thank the Nascent Transcriptomics Core at Harvard Medical School, Boston, MA for performing PRO-seq library construction and for assistance with data analysis.

Authors' Disclosures:

S.A.A. is supported by NIH grants CA259273, CA066996, and CA206963. H.J.U. is supported by the Charles A. King Foundation as well as the Mark Foundation. L.B. is supported by the Associazione Italiana per la Ricerca sul Cancro (AIRC) Start-Up Grant 22895.

S.A.A. has been a consultant and/or shareholder for Neomorph Inc, Imago Biosciences, Vitae/Allergan Pharma, Cyteir Therapeutics, Twentyeight-seven therapeutics, C4 Therapeutics, Accent Therapeutics, and Mana Therapeutics. S.A.A. has received research support from Janssen, Novartis, and Syndax. S.A.A. is an inventor on patent applications related to Menin inhibition WO/2017/132398A1. L.B. declares advisory board consultancy for Amgen and Abbvie.

Data availability statement:

All data and materials will be made available by authors upon request. RNA-seq, ChIP-seq, SLAM-seq, and PRO-seq data generated for this study have been deposited at GEO (GSE196480).

References:

1. Döhner H, Weisdorf DJ, Bloomfield CD. Acute Myeloid Leukemia. N Engl J Med. 2015;373:1136–52. [PubMed: 26376137]
2. Papaemmanuil E, Gerstung M, Bullinger L, Gaidzik VI, Paschka P, Roberts ND, et al. Genomic Classification and Prognosis in Acute Myeloid Leukemia. N Engl J Med. 2016;374:2209–21. [PubMed: 27276561]
3. Falini B, Brunetti L, Sportoletti P, Paola Martelli M. NPM1-mutated acute myeloid leukemia: from bench to bedside. Blood. 2020;136:1707–21. [PubMed: 32609823]
4. Falini B, Mecucci C, Tiacci E, Alcalay M, Rosati R, Pasqualucci L, et al. Cytoplasmic nucleophosmin in acute myelogenous leukemia with a normal karyotype. N Engl J Med. 2005;352:254–66. [PubMed: 15659725]
5. Gu X, Ebrahem Q, Mahfouz RZ, Hasipek M, Enane F, Radivoyevitch T, et al. Leukemogenic nucleophosmin mutation disrupts the transcription factor hub that regulates granulomonocytic fates. J Clin Invest. 2018;128:4260–79. [PubMed: 30015632]
6. Colombo E, Marine JC, Danovi D, Falini B, Pelicci PG. Nucleophosmin regulates the stability and transcriptional activity of p53. Nat Cell Biol. 2002;4:529–33. [PubMed: 12080348]
7. Wang AJ, Han Y, Jia N, Chen P, Minden MD. NPM1c impedes CTCF functions through cytoplasmic mislocalization in acute myeloid leukemia. Leuk 2019 345. 2019;34:1278–90.
8. Oka M, Mura S, Otani M, Miyamoto Y, Nogami J, Maehara K, et al. Chromatin-bound CRM1 recruits SET-Nup214 and NPM1c onto HOX clusters causing aberrant HOX expression in leukemia cells. Elife. 2019;8.
9. Uckelmann HJ, Kim SM, Wong EM, Hatton C, Giovinazzo H, Gadrey JY, et al. Therapeutic targeting of preleukemia cells in a mouse model of NPM1 mutant acute myeloid leukemia. Science (80-). 2020;367:586–90.
10. Kühn MWM, Song E, Feng Z, Sinha A, Chen C-W, Deshpande AJ, et al. Targeting Chromatin Regulators Inhibits Leukemogenic Gene Expression in NPM1 Mutant Leukemia. Cancer Discov. 2016;6:1166–81. [PubMed: 27535106]
11. Krivtsov A V, Evans K, Gadrey JY, Eschle BK, Hatton C, Uckelmann HJ, et al. A Menin-MLL Inhibitor Induces Specific Chromatin Changes and Eradicates Disease in Models of MLL-Rearranged Leukemia. Cancer Cell. 2019;36:660–673.e11. [PubMed: 31821784]
12. Yokoyama A, Cleary ML. Menin Critically Links MLL Proteins with LEDGF on Cancer-Associated Target Genes. Cancer Cell. 2008;14:36–46. [PubMed: 18598942]
13. Klossowski S, Miao H, Kempinska K, Wu T, Purohit T, Kim E, et al. Menin inhibitor MI-3454 induces remission in MLL1-rearranged and NPM1-mutated models of leukemia. J Clin Invest. 2020;130:981–97. [PubMed: 31855575]

14. Brunetti L, Gundry MC, Sorcini D, Guzman AG, Huang YH, Ramabadran R, et al. Mutant NPM1 Maintains the Leukemic State through HOX Expression. Cancer Cell. 2018;34:499–512.e9. [PubMed: 30205049]
15. Nabet B, Roberts JM, Buckley DL, Paulk J, Dastjerdi S, Yang A, et al. The dTAG system for immediate and target-specific protein degradation. Nat Chem Biol. 2018;14:431–41. [PubMed: 29581585]
16. Ley TJ, Miller C, Ding L, Raphael BJ, Mungall AJ, Robertson G, et al. Genomic and epigenomic landscapes of adult de novo acute myeloid leukemia. N Engl J Med. 2013;368:2059–74. [PubMed: 23634996]
17. Network TCGAR. Genomic and Epigenomic Landscapes of Adult De Novo Acute Myeloid Leukemia. N Engl J Med. 2013;368:2059–74. [PubMed: 23634996]
18. Wouters BJ, Löwenberg B, Erpelinck-Verschueren CAJ, Van Putten WLJ, Valk PJM, Delwel R. Double CEBPA mutations, but not single CEBPA mutations, define a subgroup of acute myeloid leukemia with a distinctive gene expression profile that is uniquely associated with a favorable outcome. Blood. 2009;113:3088–91. [PubMed: 19171880]
19. Tyner JW, Tognon CE, Bottomly D, Wilmot B, Kurtz SE, Savage SL, et al. Functional genomic landscape of acute myeloid leukaemia. Nat 2018 5627728. 2018;562:526–31.
20. Muhar M, Ebert A, Neumann T, Umkehrer C, Jude J, Wieshofer C, et al. SLAM-seq defines direct gene-regulatory functions of the BRD4-MYC axis. Science (80-). 2018;360:800–5.
21. Mahat DB, Kwak H, Booth GT, Jonkers IH, Danko CG, Patel RK, et al. Base-pair-resolution genome-wide mapping of active RNA polymerases using precision nuclear run-on (PRO-seq). Nat Protoc 2016 118. 2016;11:1455–76.
22. Kwak H, Fuda NJ, Core LJ, Lis JT. Precise maps of RNA polymerase reveal how promoters direct initiation and pausing. Science. 2013;339:950–3. [PubMed: 23430654]
23. Zhao Y, Liu Q, Acharya P, Stengel KR, Sheng Q, Zhou X, et al. High-Resolution Mapping of RNA Polymerases Identifies Mechanisms of Sensitivity and Resistance to BET Inhibitors in t(8;21) AML. Cell Rep. 2016;16:2003–16. [PubMed: 27498870]
24. Peng J, Liu M, Marion J, Zhu Y, Price DH. RNA Polymerase II Elongation Control. Cold Spring Harb Symp Quant Biol. 1998;63:365–70. [PubMed: 10384301]
25. Shi J, Wang E, Milazzo JP, Wang Z, Kinney JB, Vakoc CR. Discovery of cancer drug targets by CRISPR-Cas9 screening of protein domains. Nat Biotechnol 2015 336. 2015;33:661–7.
26. Hingorani K, Szebeni A, Olson MOJ. Mapping the functional domains of nucleolar protein B23. J Biol Chem. 2000;275:24451–7. [PubMed: 10829026]
27. Falini B, Nicoletti I, Bolli N, Martelli MP, Liso A, Gorello P, et al. Translocations and mutations involving the nucleophosmin (NPM1) gene in lymphomas and leukemias. Haematologica. 2007;92:519–32. [PubMed: 17488663]
28. Murano K, Okuwaki M, Hisaoka M, Nagata K. Transcription regulation of the rRNA gene by a multifunctional nucleolar protein, B23/nucleophosmin, through its histone chaperone activity. Mol Cell Biol. 2008;28:3114–26. [PubMed: 18332108]
29. Shandilya J, Swaminathan V, Gadad SS, Choudhari R, Kodaganur GS, Kundu TK. Acetylated NPM1 localizes in the nucleoplasm and regulates transcriptional activation of genes implicated in oral cancer manifestation. Mol Cell Biol. 2009;29:5115–27. [PubMed: 19581289]
30. Escobar TM, Yu JR, Liu S, Lucero K, Vasilyev N, Nudler E, et al. Inheritance of repressed chromatin domains during S phase requires the histone chaperone NPM1. Sci Adv. 2022;8.
31. Brunetti L, Gundry MC, Goodell MA. New insights into the biology of acute myeloid leukemia with mutated NPM1. International Journal of Hematology. 2019;110:150–60. [PubMed: 30632059]
32. Oka M, Mura S, Otani M, Miyamoto Y, Nogami J, Maehara K, et al. Chromatin-bound CRM1 recruits SET-Nup214 and NPM1c onto HOX clusters causing aberrant HOX expression in leukemia cells. Elife. 2019;8.
33. Olsen SN, Godfrey L, Healy JP, Choi YA, Kai Y, Hatton C, et al. MLL::AF9 degradation induces rapid changes in transcriptional elongation and subsequent loss of an active chromatin landscape. Mol Cell. 2022;82:1140–1155.e11. [PubMed: 35245435]

34. Pianigiani G, Gagliardi A, Mezzasoma F, Rocchio F, Tini V, Bigerna B, et al. Prolonged XPO1 inhibition is essential for optimal antileukemic activity in NPM1-mutated AML. Blood Adv. 2022. 8.
35. Grisendi S, Mecucci C, Falini B, Pandolfi PP. Nucleophosmin and cancer. Nat Rev Cancer 2006 67. 2006;6:493–505.
36. Colombo E, Martinelli P, Zamponi R, Shing DC, Bonetti P, Luzi L, et al. Delocalization and Destabilization of the Arf Tumor Suppressor by the Leukemia-Associated NPM Mutant. Cancer Res. 2006;66:3044–50. [PubMed: 16540653]
37. Gu X, Ebrahem Q, Mahfouz RZ, Hasipek M, Enane F, Radivoyevitch T, et al. Leukemogenic nucleophosmin mutation disrupts the transcription factor hub that regulates granulomonocytic fates. J Clin Investig. 2018;128:4260–79. [PubMed: 30015632]
38. Swaminathan V, Kishore AH, Febitha KK, Kundu TK. Human Histone Chaperone Nucleophosmin Enhances Acetylation-Dependent Chromatin Transcription. Mol Cell Biol. 2005;25:7534–45. [PubMed: 16107701]
39. Yogev O, Saadon K, Anzi S, Inoue K, Shaulian E. DNA damage-dependent translocation of B23 and p19 ARF is regulated by the Jun N-terminal kinase pathway. Cancer Res. 2008;68:1398–406. [PubMed: 18316603]
40. Lee SY, Park JH, Kim S, Park EJ, Yun Y, Kwon J. A proteomics approach for the identification of nucleophosmin and heterogeneous nuclear ribonucleoprotein C1/C2 as chromatin-binding proteins in response to DNA double-strand breaks. Biochem J. 2005;388 Pt 1:7–15. [PubMed: 15737070]
41. MacPherson L, Anokye J, Yeung MM, Lam EYN, Chan YC, Weng CF, et al. HBO1 is required for the maintenance of leukaemia stem cells. Nature. 2020;577:266–70. [PubMed: 31827282]
42. Yan F, Li J, Milosevic J, Petroni R, Liu S, Shi Z, et al. KAT6A and ENL Form an Epigenetic Transcriptional Control Module to Drive Critical Leukemogenic Gene-Expression Programs. Cancer Discov. 2022;12:792–811. [PubMed: 34853079]
43. Krivtsov A V, Hoshii T, Armstrong SA. Mixed-Lineage Leukemia Fusions and Chromatin in Leukemia. Cold Spring Harb Perspect Med. 2017;7:a026658. [PubMed: 28242784]
44. Bach C, Buhl S, Mueller D, Garcia-Cuellar MP, Maethner E, Slany RK. Leukemogenic transformation by HOXA cluster genes. Blood. 2010;115:2910–8. [PubMed: 20130239]
45. Wang GG, Pasillas MP, Kamps MP. Persistent Transactivation by Meis1 Replaces Hox Function in Myeloid Leukemogenesis Models: Evidence for Co-Occupancy of Meis1-Pbx and Hox-Pbx Complexes on Promoters of Leukemia-Associated Genes. Mol Cell Biol. 2006;26:3902–16. [PubMed: 16648484]
46. Townsend EC, Murakami MA, Christodoulou A, Christie AL, Köster J, DeSouza TA, et al. The Public Repository of Xenografts Enables Discovery and Randomized Phase II-like Trials in Mice. Cancer Cell. 2016;29:574–86. [PubMed: 27070704]
47. Mohammed H, Taylor C, Brown GD, Papachristou EK, Carroll JS, D'Santos CS. Rapid immunoprecipitation mass spectrometry of endogenous proteins (RIME) for analysis of chromatin complexes. Nat Protoc 2015 112. 2016;11:316–26.
48. Reimer KA, Mimoso CA, Adelman K, Neugebauer KM. Co-transcriptional splicing regulates 3' end cleavage during mammalian erythropoiesis. Mol Cell. 2021;81:998–1012.e7. [PubMed: 33440169]
49. Neumann T, Herzog VA, Muhar M, Von Haeseler A, Zuber J, Ameres SL, et al. Quantification of experimentally induced nucleotide conversions in high-throughput sequencing datasets. BMC Bioinformatics. 2019;20:1–16. [PubMed: 30606105]

STATEMENT OF SIGNIFICANCE

We uncovered an important functional role of mutant NPM1 as a crucial direct driver of oncogenic gene expression in acute myeloid leukemia. NPM1c can bind to chromatin and cooperate with the MLL complex, providing the first functional insight into the mechanism of Menin-MLL inhibition in NPM1c leukemias.

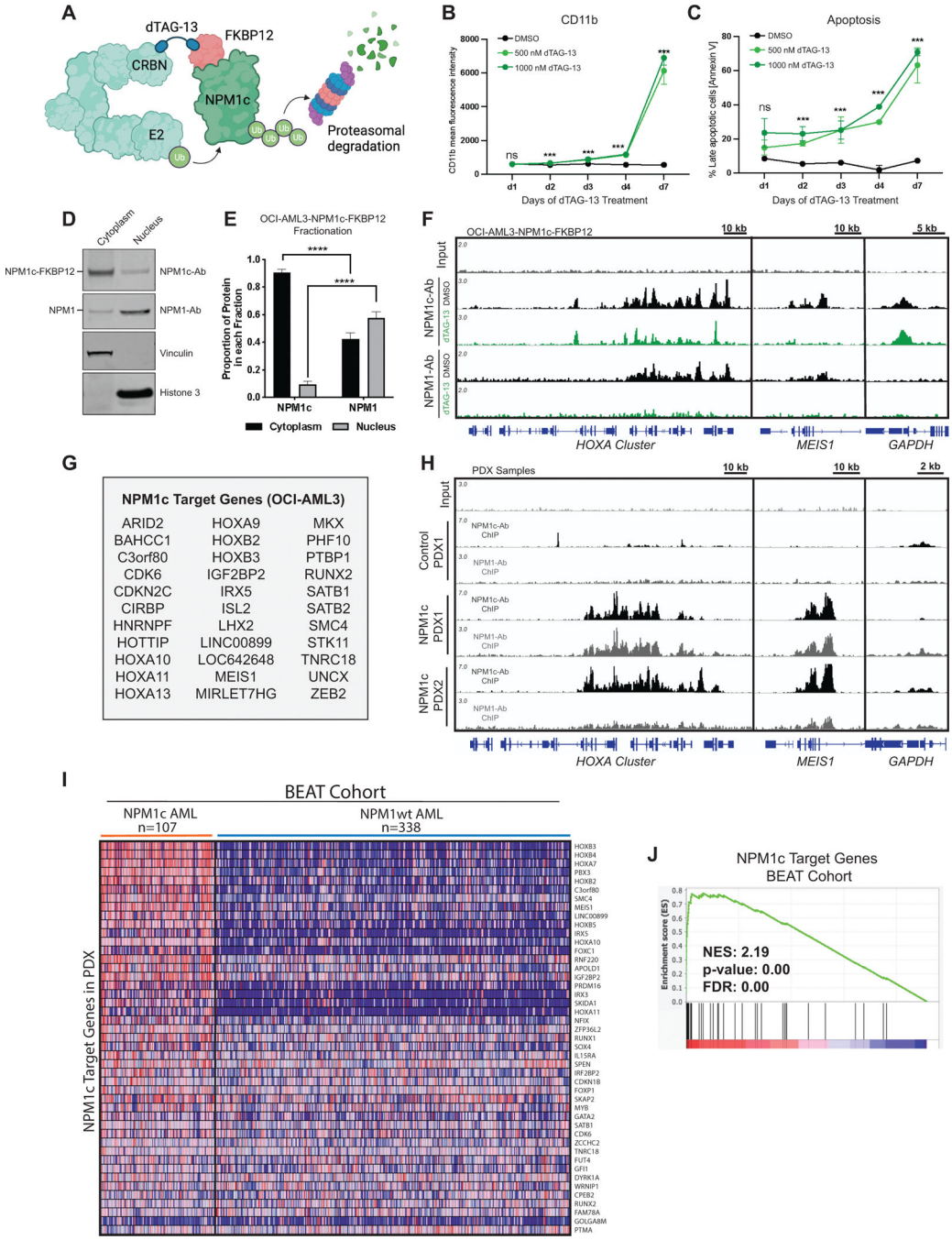

Figure 1. Identification of NPM1c chromatin targets through targeted degradation.

A, Experimental overview of dTAG system. B, CD11b mean fluorescence intensity after 1 to 7 days of dTAG-13 treatment (500 nM) determined by FACS. Representative experiment of n=3 biological replicates. n=3 technical replicates plotted. C, Percent of Annexin V and DAPI double positive apoptotic cells determined by FACS. Representative experiment of n=3 biological replicates. n=3 technical replicates plotted. D, Representative immunoblot of 40 ug of cytoplasmic and nuclear fractions of OCI-AML3-NPM1c-FKBP12 cells probed for mutant NPM1c, total NPM1, Vinculin, and Histone 3. E, Quantification of NPM1c-Ab

and NPM1-Ab bands from n=4 biological replicates of immunoblot of cytoplasmic and nuclear fractions from OCI-AML3-NPM1c-FKBP12 cells. F, Gene tracks of NPM1c-Ab and NPM1-Ab ChIPseq signal following 24 hours of dTAG-13 treatment (500 nM) in OCI-AML3-NPM1c-FKBP12 cells. Representative plot of n=2 biological replicates shown. G, List of NPM1c chromatin targets in OCI-AML3 cells. H, Gene tracks of ChIPseq signal of an NPM1 wildtype control PDX and two NPM1c mutant PDX using NPM1c-Ab and NPM1-Ab. I, Heatmap showing gene expression changes of PDX derived NPM1c targets in NPM1c versus wildtype NPM1 patient samples from the BEAT AML cohort. J, Gene set enrichment analysis showing enrichment of the expression of PDX specific NPM1c target genes (n=54, Supplementary Table S2) in NPM1c compared to NPM1wt patient samples from publicly available gene expression data from the BEAT AML cohort. ns $p > 0.5$; *p % 0.05; **p % 0.01; ***p % 0.001; and ****p % 0.001 (Mann-Whitney test).

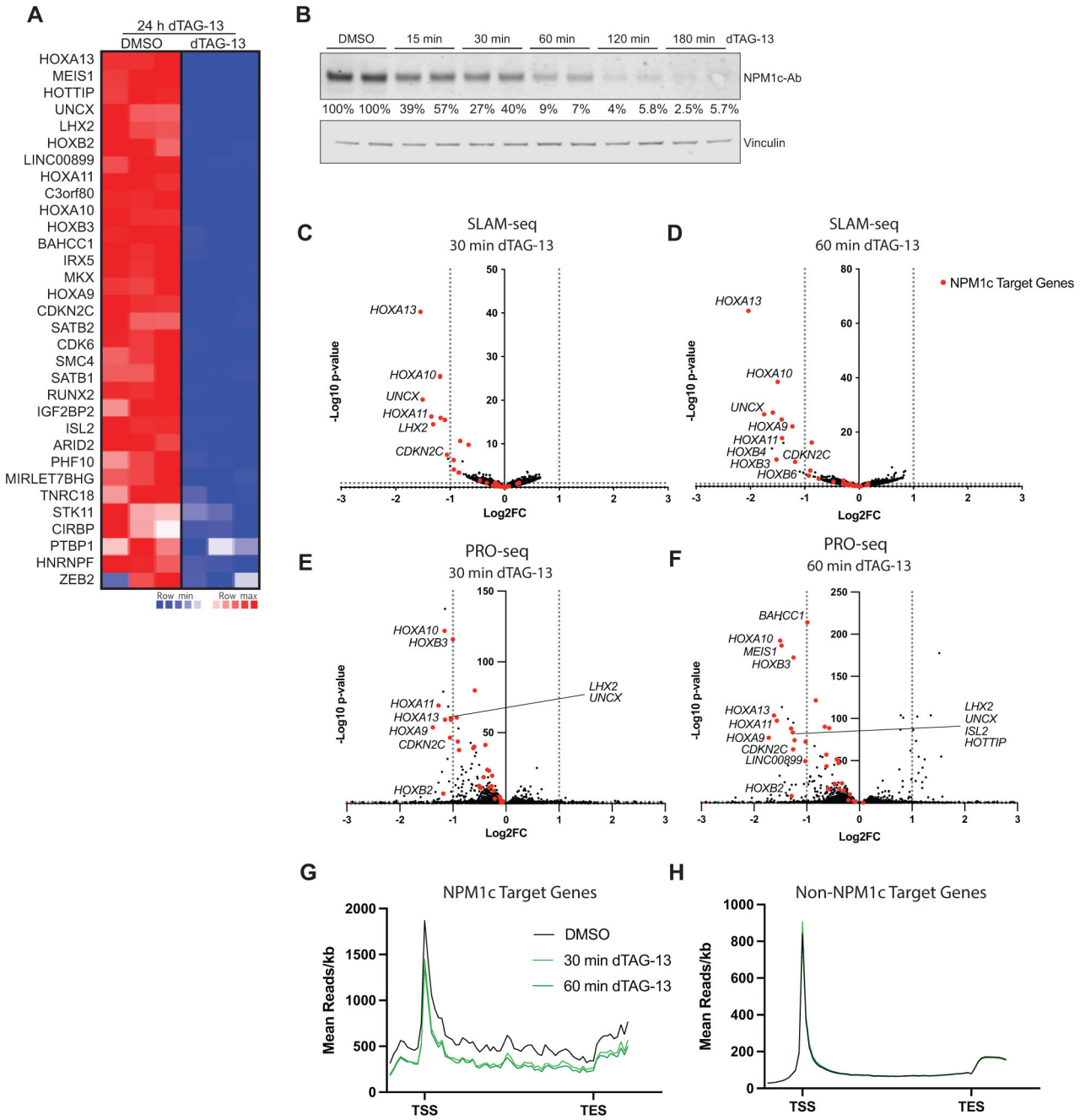

Figure 2. NPM1c regulates transcription of its chromatin targets.

A, Heatmap of differentially expressed NPM1c target genes at 24 hours post dTAG-13 treatment (500 nM) as measured by RNAseq in OCI-AML3-NPM1c-FKBP12 cells. B, Immunoblot of cell lysate from OCI-AML3-NPM1c-FKBP12 cells treated with dTAG-13 (500 nM) for 15, 30, 60, 120, and 180 min probed with NPM1c-Ab and anti-Vinculin. n=2 technical replicates. C and D, Volcano plot of SLAM-seq data showing −log10 P-values versus log2 fold changes in OCI-AML3-NPM1c-FKBP12 cells 30 minutes (C) or 60 minutes (D) post dTAG-13 treatment (500 nM). n=3 biological replicates. E and F, Volcano plot of PRO-seq data showing −log10 P-values versus log2 fold changes in OCI-AML3-

NPM1c-FKBP12 cells 30 minutes (E) or 60 minutes (F) post dTAG-13 treatment (500 nM). n=2 biological replicates. G, Average metagene plots of PRO-seq read density from TSS to TES of NPM1c target genes after dTAG-13 treatment (500 nM). n=2 biological replicates. H, Average metagene plots of PRO-seq read density from TSS to TES of non-NPM1 target genes after dTAG-13 treatment (500 nM). n=2 biological replicates.

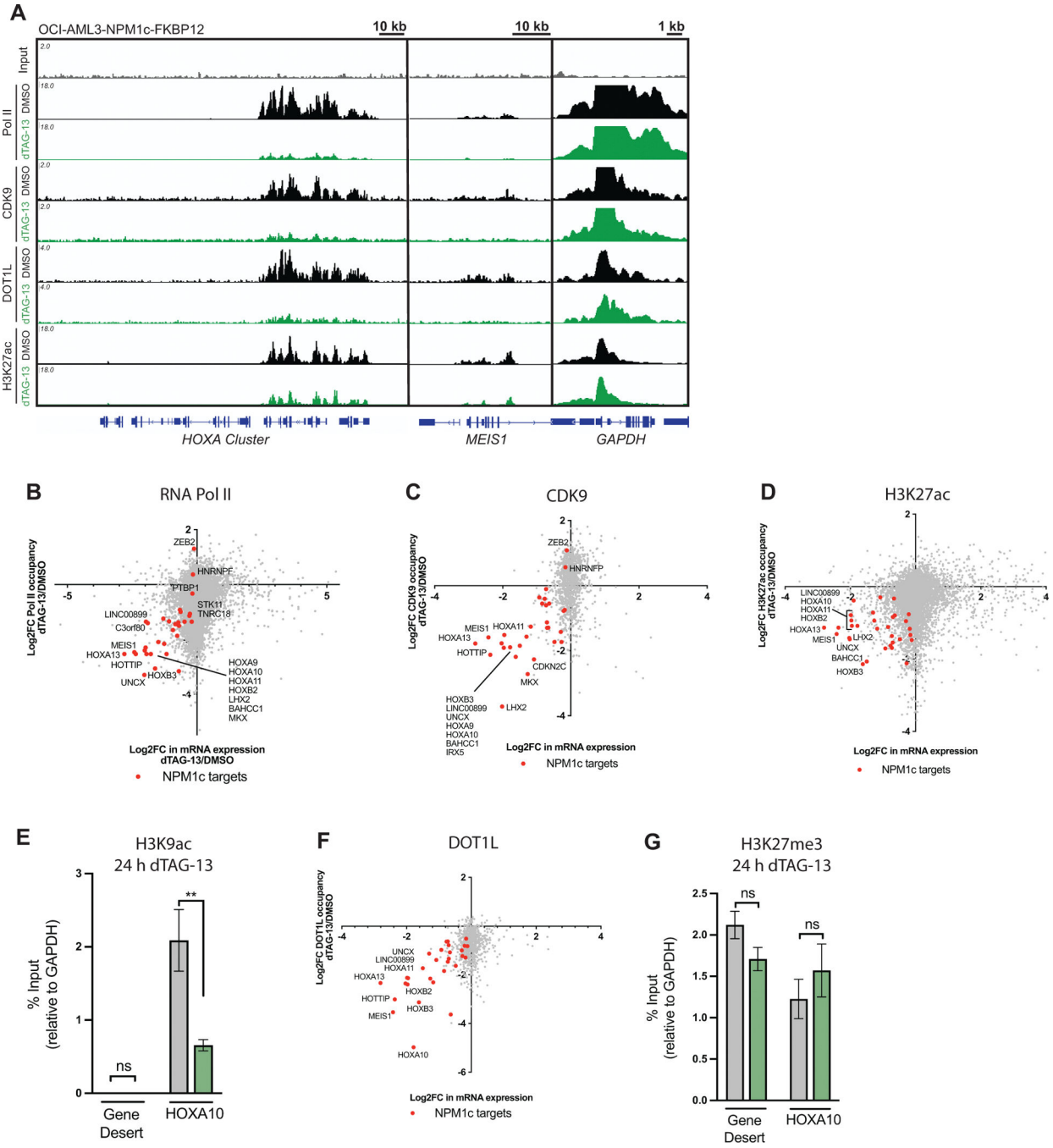

Figure 3. NPM1c loss induces rapid changes in chromatin occupancy of Pol II and CDK9.

A, Gene tracks of Pol II, CDK9, DOT1L, and H3K27ac ChIPseq signal following 24 hours of DMSO or dTAG-13 treatment (500 nM) in OCI-AML3-NPM1c-FKBP12 cells. Representative plot from n=2 biological replicates shown. B-D, Log2 fold change of RNA Pol II (B), CDK9 (C), and H3K27ac (D) ChIPseq signal versus gene expression (RNAseq) of OCI-AML3-NPM1c-FKBP12 cells treated with dTAG-13 (500 nM) for 24 h. NPM1c targets labeled in red. Representative plot from n=2 biological replicates shown. E, ChIP qPCR of H3K9ac after 24 h of dTAG-13 treatment (500 nM) in OCI-AML3-NPM1c-

FKBP12 cells. HOXA9 and Gene desert are shown relative to GAPDH. Data represent the mean and standard deviation of n=3 technical replicates. F, Log2 fold change of DOT1L versus gene expression (RNAseq) of OCI-AML3-NPM1c-FKBP12 cells treated with dTAG-13 (500 nM) for 24 h. NPM1c targets labeled in red. Representative plot from n=2 biological replicates shown. G, ChIP qPCR of H3K27me3 after 24 h of dTAG-13 treatment (500 nM) in OCI-AML3-NPM1c-FKBP12 cells. HOXA10 and Gene desert are shown relative to GAPDH. Data represent the mean and standard deviation of n=3 technical replicates. ns p > 0.5; *p % 0.05; **p % 0.01; ***p % 0.001; and ****p % 0.001 (Mann-Whitney test).

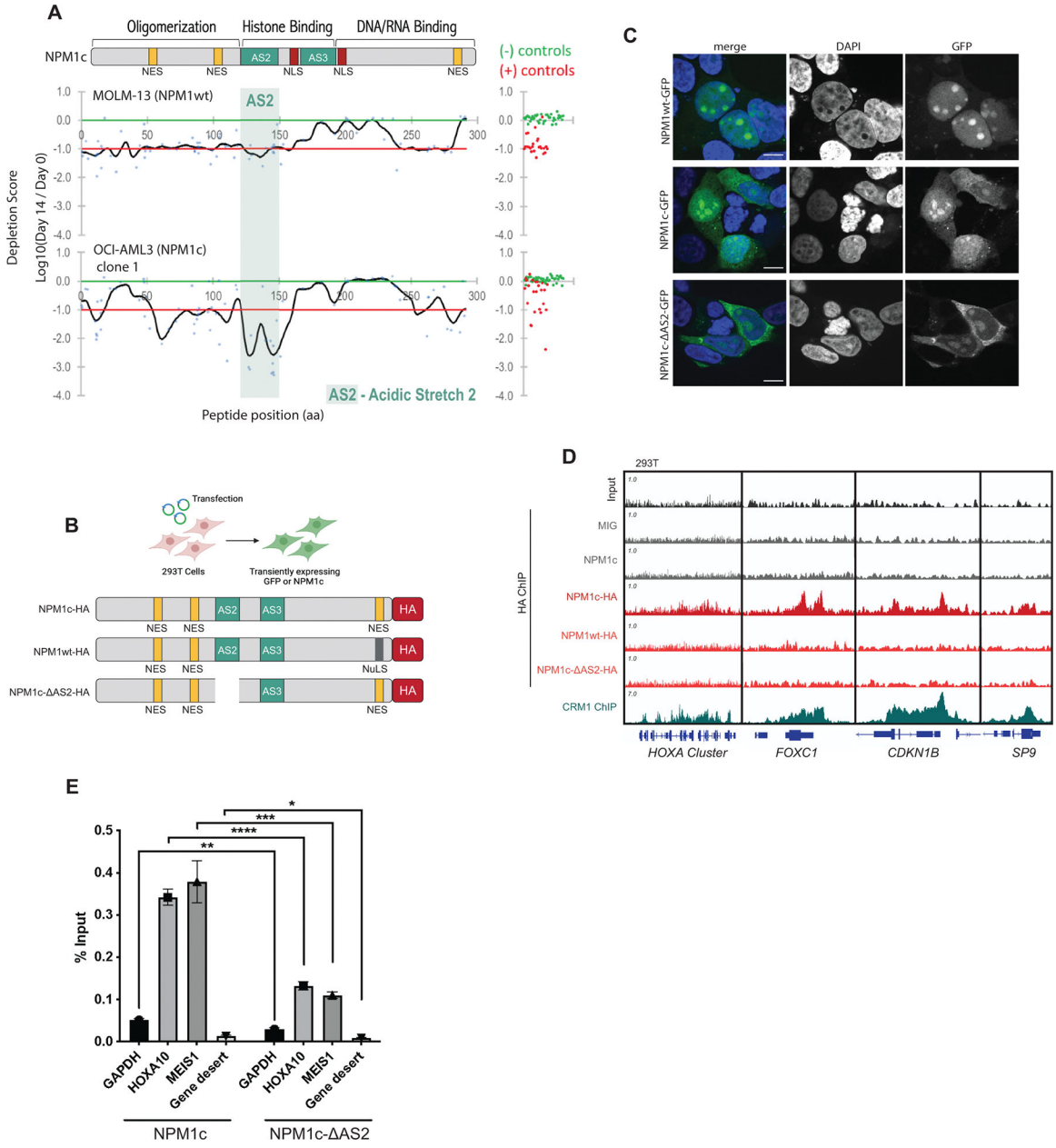

Figure 4. NPM1c chromatin binding is mediated by acidic stretch 2.

A, CRISPR domain scanning score of each sgRNA (dots) and smoothened score (line) of NPM1c tiling screen in OCI-AML3-Cas9 single cell clone 1 or MOLM13-Cas9 cells at 14 days of culture. Negative control sgRNAs shown in green, killing control sgRNAs shown in red. CRISPR Screen was performed in two independent single cell OCI-AML3-Cas9 clones, representative plot shown. B, Experimental overview of transient overexpression of different NPM1c mutants in 293T cells. C, Maximum intensity projection images of confocal stacks of 293T cells expressing NPM1wt-GFP, NPM1c-GFP, or NPM1c-ΔAS2-GFP stained with DAPI. Scale bar 10 μm. D, Gene tracks of HA ChIPseq signal of 293T cells overexpressing control MIG, NPM1c, NPM1c-HA, NPM1wt-HA, or NPM1c-ΔAS2-HA. CRM1 ChIPseq signal gene tracks shown from untransfected 293T cells. Representative plot of n=2

biological replicates shown. E, ChIP qPCR of NPM1c-Ab after 24 h of dTAG-13 treatment (500 nM) in OCI-AML3-NPM1c-FKBP12 cells expressing NPM1c or NPM1c-ΔAS2. Data represent the mean and standard deviation of n=3 technical replicates. Representative plot from n=2 biological replicates shown. ns p > 0.5; *p % 0.05; **p % 0.01; ***p % 0.001; and ****p % 0.001 (Mann-Whitney test).

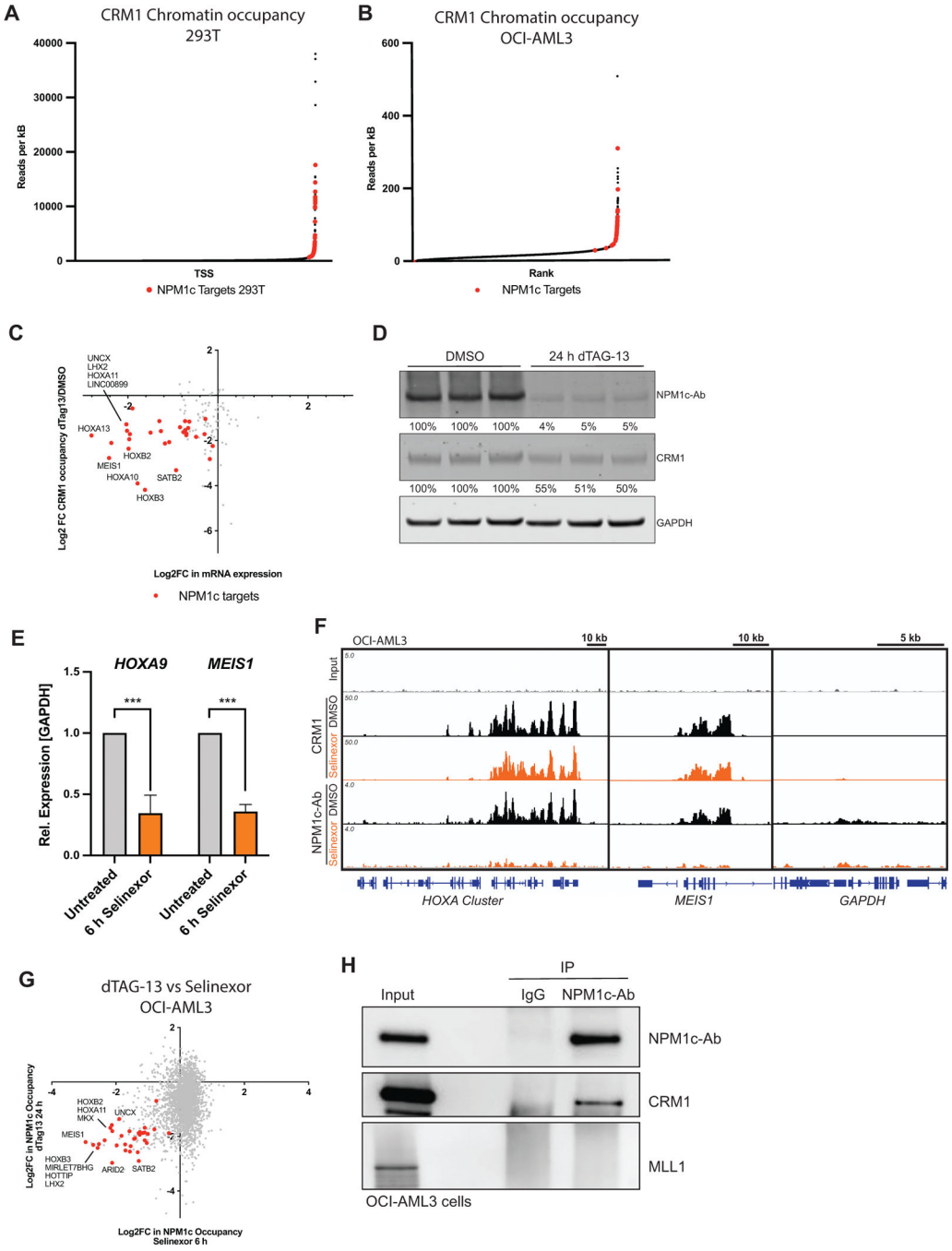

Figure 5. CRM1 is important for the genome-wide chromatin recruitment of NPM1c.

A, CRM1 chromatin loading determined by CRM1 ChIPseq in 293T cells. 293T specific NPM1c targets labeled in red. B, CRM1 chromatin loading determined by CRM1 ChIPseq in OCI-AML3 cells. OCI-AML3 specific NPM1c targets labeled in red. Representative plot of n=2 biological replicates shown. Representative plot of n=2 biological replicates shown. C, Log2 fold change of CRM1 ChIPseq signal versus gene expression (RNAseq) of OCI-AML3-NPM1c-FKBP12 cells treated with dTAG-13 (500 nM) for 24 h. NPM1c targets labeled in red. D, Immunoblot showing NPM1c, CRM1, and GAPDH protein levels 24 h

post dTAG-13 treatment (500nM) in OCI-AML3-FKBP12 cells. Percentage of normalized band intensities indicated below. n=3 biological replicates. E, Relative gene expression of *HOXA9* and *MEIS1* in OCI-AML3 cells treated with Selinexor (100 nM) for 6 h. Data represent mean and standard deviation of n=3 biological replicates. F, Gene tracks of CRM1 and NPM1c-Ab ChIPseq signal from OCI-AML3 cells treated with Selinexor treatment (100 nM) for 6 hours. Representative plot of n=2 biological replicates shown. G, Log2 fold change in NPM1c-Ab ChIPseq signal after 24 h dTAG-13 (500 nM) in OCI-AML3-NPM1c-FKBP12 versus 6 h Selinexor treatment OCI-AML3. NPM1c targets labeled in red. Representative plot of n=2 biological replicates shown. H, Immunoblot of co-immunoprecipitation of NPM1c-Ab from the chromatin fraction of OCI-AML3 cells probed for NPM1c, CRM1, and MLL1. Representative immunoblot of n=3 biological replicates shown. ns p > 0.5; *p % 0.05; **p % 0.01; ***p % 0.001; and ****p % 0.001 (Mann-Whitney test).

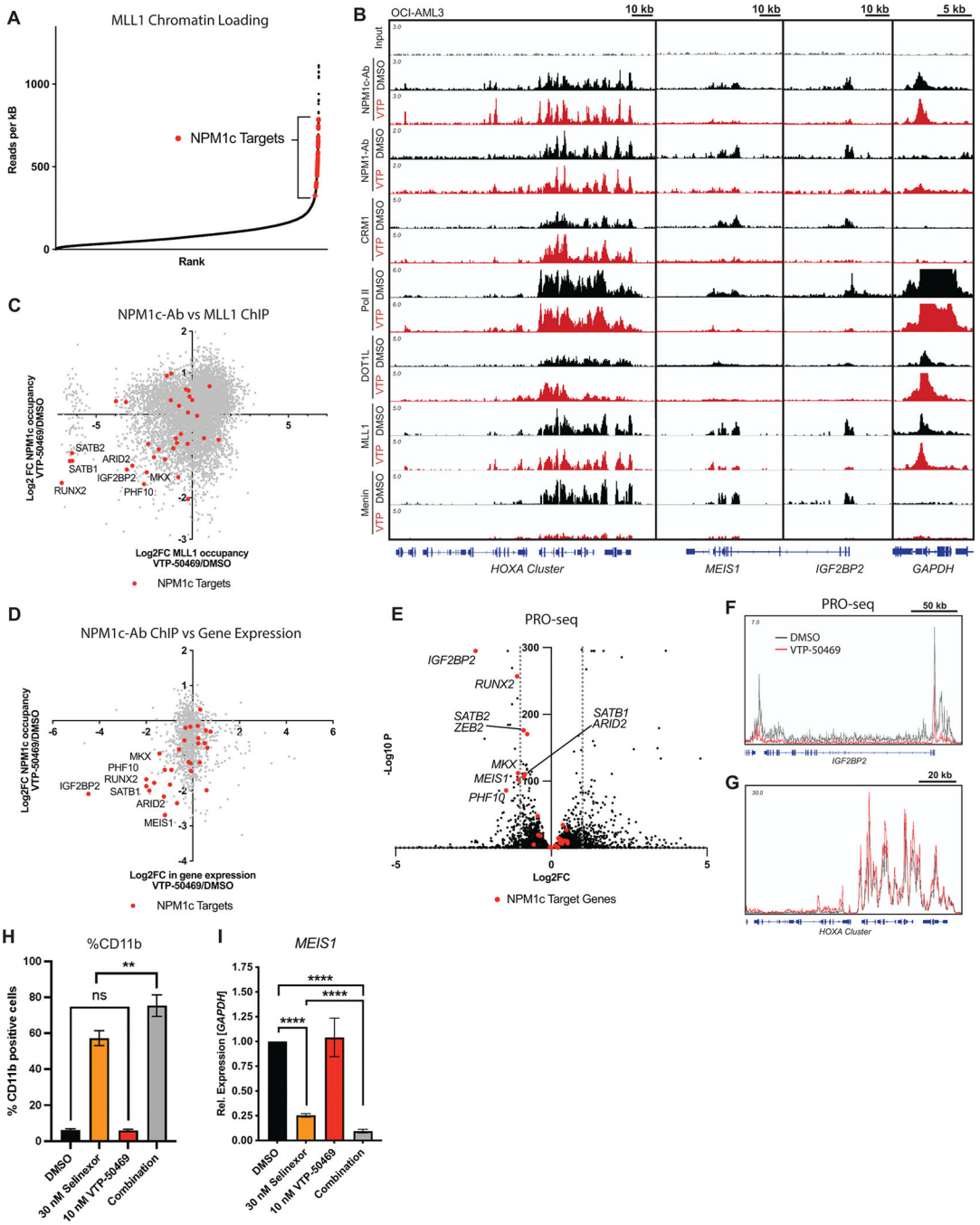

Figure 6. NPM1c chromatin occupancy is dependent on Menin-MLL interaction.

A, MLL1 chromatin loading in OCI-AML3 cells determined by ChIPseq. NPM1c targets labeled in red. Representative plot of n=3 biological replicates shown. B, Gene tracks of NPM1c-Ab, NPM1-Ab, CRM1, Pol II, DOT1L, MLL1, and Menin ChIPseq signal following 4 days of VTP-50469 treatment (330 nM) in OCI-AML3 cells. MLL1 and Menin ChIPseq data from previously published study (GSE129638) were used. C, Log2 fold change of NPM1c occupancy versus MLL1 occupancy determined by ChIPseq after 4 days of VTP-50469 treatment (330 nM) in OCI-AML3 cells. NPM1c targets labeled

in red. Representative plot of n=2 biological replicates shown. D, Log2 fold change of NPM1c occupancy determined by ChIPseq versus gene expression (RNAseq) after 4 days of VTP-50469 treatment (330 nM) in OCI-AML3 cells. NPM1c targets labeled in red. Representative plot of n=2 biological replicates shown. E, Volcano plot of PRO-seq data showing −log10 P-values versus log2 fold changes in OCI-AML3-NPM1c-FKBP12 cells 48 hours post VTP-50469 treatment (330 nM). NPM1c targets labeled in red. n=2 biological replicates. F and G, PRO-seq read density at *IGF2BP2* locus (F) and *HOXA* cluster (G) 48 hours post VTP-50469 treatment (330 nM). n=2 biological replicates. H, Representative experiment of n=3 biological replicates of CD11b surface expression of OCI-AML3 cells treated with Selinexor (30 nM), VTP-50469 (10 nM), or both for 3 days. n=3 technical replicates plotted. I, *MEIS1* gene expression analysis of OCI-AML3 cells treated with Selinexor (30 nM), VTP-50469 (10 nM), or both for 3 days, normalized to DMSO. Data represent the mean and standard deviation of n=4 biological replicates. ns p > 0.5; *p % 0.05; **p % 0.01; ***p % 0.001; and ****p % 0.001 (Mann-Whitney test).